

מכון ויצמן למדע

WEIZMANN INSTITUTE OF SCIENCE



Designer protein assemblies with tunable phase diagrams in living cells

Document Version:

Accepted author manuscript (peer-reviewed)

Citation for published version:

Heidenreich, M, Georgeson, JM, Locatelli, E, Rovigatti, L, Nandi, SK, Steinberg, A, Nadav, Y, Shimoni, E, Safran, SA, Doye, JPK & Levy, ED 2020, 'Designer protein assemblies with tunable phase diagrams in living cells', *Nature Chemical Biology*, vol. 16, no. 9, pp. 939-945. <https://doi.org/10.1038/s41589-020-0576-z>

Total number of authors:

11

Digital Object Identifier (DOI):

[10.1038/s41589-020-0576-z](https://doi.org/10.1038/s41589-020-0576-z)

Published In:

Nature Chemical Biology

License:

Other

General rights

@ 2020 This manuscript version is made available under the above license via The Weizmann Institute of Science Open Access Collection is retained by the author(s) and / or other copyright owners and it is a condition of accessing these publications that users recognize and abide by the legal requirements associated with these rights.

How does open access to this work benefit you?

Let us know @ library@weizmann.ac.il

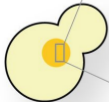
Take down policy

The Weizmann Institute of Science has made every reasonable effort to ensure that Weizmann Institute of Science content complies with copyright restrictions. If you believe that the public display of this file breaches copyright please contact library@weizmann.ac.il providing details, and we will remove access to the work immediately and investigate your claim.

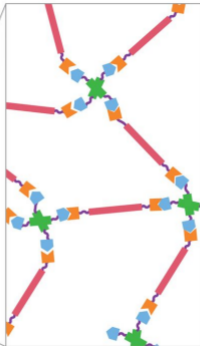
Synthetic Proteins



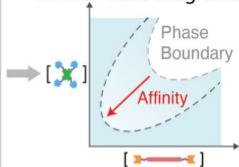
+



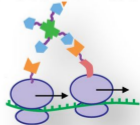
Yeast



In vivo Phase Diagrams



mRNA Localization by Co-Translational Assembly



1
2
3
4

1. Extended Data

Figure #	Figure title One sentence only	Filename This should be the name the file is saved as when it is uploaded to our system. Please include the file extension. i.e.: <i>Smith_ED_Fig1.jpg</i>	Figure Legend If you are citing a reference for the first time in these legends, please include all new references in the main text Methods References section, and carry on the numbering from the main References section of the paper. If your paper does not have a Methods section, include all new references at the end of the main Reference list.
Extended Data Fig. 1	The components do not form condensates when expressed individually.	Extended_data_fig_1-01.jpg	Haploid cells expressing only one of the building blocks show a homogenous distribution of fluorescence throughout the cytoplasm. The left-most image shows cells expressing the dimer component lacking the Im2 domain. The next images show cells expressing the variants of the dimer component in the absence of the tetramer component. The right-most image shows cells expressing the tetramer component in the absence of the dimer component. This result was replicated three times.
Extended Data Fig. 2	The synthetic condensates are not membrane-bound.	Extended_data_fig_2-01.jpg	a. Transmission electron microscopy (TEM) micrograph of fixed and sectioned yeast shows a condensate formed by our minimal system, in the cytoplasm. b. The yellow arrow points to one of several 10 nm gold-labeled anti-GFP antibodies, confirming the identity of the designed compartments. White arrows highlight the lack of membrane surrounding the compartment. c. Scanning electron microscopy micrograph of cells frozen at high-pressure and cryo-fractured reveals the mosaic of amorphous cytoplasm. The region outlined by white carets exhibits a distinct ultrastructure d. Increased magnification of a suspected condensate within the cytoplasm, outlined with white carets. This ultrastructure has no visible membrane. Scale bar 1 μm . We did not carry independent biological replicates of these electron microscopy experiments.
Extended Data Fig. 3	Impact of affinity on the phase diagram of the dimer-tetramer system.	Extended_data_fig_3-01.jpg	a. We used a lattice model (Supplementary Note, Section 1) of the dimer-tetramer system. In the square lattice, concentration is measured by fractional occupancy of edges and vertices by dimers and tetramers respectively. We calculated the binodal of this system in the plane corresponding to the fractional occupancy of dimer (x-axis) and tetramer (y-axis). Affinity increases in panels from left to right, where μ is the binding energy in units of kT of a linker and one arm of the tetravalent molecule. Higher

			affinity (larger μ) increases the fraction of the phase-separated region. b. We used mean-field theoretical calculations of patchy particles matching the geometry of the proteins. The binodal is calculated in the plane corresponding to the concentration of dimers (x-axis) and tetramers (y-axis). Affinity (which is linked to the energy and entropy associated with the formation of a bond, see Supplementary Note, Section 1) increases from left to right.
Extended Data Fig. 4	Simulations recapitulate the kinetic trapping effect observed experimentally.	Extended_data_fig_4-01.jpg	a. Sedimentation molecular dynamics simulation of patchy particles. Several simulations were conducted at equilibrium or out-of-equilibrium while sampling different concentrations of dimer and tetramer. The protein osmotic pressure as a function of density was inferred from each simulation and used to evaluate the phase boundaries. b. The phase diagram of the patchy mixture computed with equilibrium and non-equilibrium simulations (squares and circles, respectively).
Extended Data Fig. 5	<i>In vivo</i> phase diagrams and fluorescence recovery profiles observed with different affinities.	Extended_data_fig_5_1-01.jpg	a. <i>In vivo</i> phase diagrams observed for five affinities investigated initially. Concentrations correspond to those of the binding sites (not of the dimer and tetramer complexes). The red line highlights the diagonal, where the concentrations of binding sites of dimer and tetramers are equal. The grey dotted lines show the lower limit of concentrations that can be reliably estimated. b. Fluorescence recovery profiles of photobleached condensates for different interaction affinities between the components. Grey lines show individual experiments, the red line corresponds to the mean recovery and the red area shows the standard error. The transparent red area indicates the standard error. The mean recovery after 25 seconds and associated standard error are given for each affinity.
Extended Data Fig. 6	Replicating the measurement of <i>in vivo</i> phase diagrams with four additional affinities.	extended_data_fig_6.jpg	Phase diagrams measured for nine affinities. Five affinities come from replicating experiments shown in Fig. S6, and four are new. Concentrations correspond to those of the binding sites (not of the dimer and tetramer complexes). The red line highlights the diagonal, where the concentrations of binding sites of dimer and tetramers are equal. The grey dotted lines show the lower limit of concentrations that can be reliably estimated. Affinities and mutations are indicated above. The N34V, R38T, double N34V/R38T and triple D33L/N34V/R38T mutants were added later to further investigate the out-of-equilibrium effect. The same number of randomly selected cells were plotted in all panels (n=4000) to allow comparing the density of points across plots.
Extended Data	The mRNA coding	Extended_data_f	Cells were treated with a final concentration of 10

Fig. 7	for the dimer is released from condensates within minutes after the addition of puromycin.	ig_7.jpg	mM puromycin and mRNA release from the condensate was followed by time-lapse microscopy.
--------	--	----------	--

5

2. Supplementary Information:

6

Item	Present?	Filename This should be the name the file is saved as when it is uploaded to our system, and should include the file extension. The extension must be .pdf	A brief, numerical description of file contents. i.e.: <i>Supplementary Figures 1-4, Supplementary Discussion, and Supplementary Tables 1-4.</i>
Supplementary Information	Yes	02_Heidenreich_et_al_SM_2020_03_29.pdf	Supplementary Tables 1-3, Supplementary Figures 1-5, Supplementary Note
Reporting Summary	Yes	nr-reporting-summary_V2.pdf	

7

8

A. Additional Supplementary Files

9

Type	Number If there are multiple files of the same type this should be the numerical indicator. i.e. "1" for Video 1, "2" for Video 2, etc.	Filename This should be the name the file is saved as when it is uploaded to our system, and should include the file extension. i.e.: <i>Smith_Supplementary_Video_1.mov</i>	Legend or Descriptive Caption Describe the contents of the file
Supplementary Video	1	Supplementary_video_1.avi	Synthetic condensates expressed in yeast cells. New synthetic condensates appear in budding daughter cells and their size grows with time. The video is representative for at least three independent experiments.
Supplementary Video	2	Supplementary_video_2.avi	FRAP on condensates. Condensates involving high (left) and low (right) affinity binding

			domains show slower (left) and faster (right) recovery after photobleaching. The video is representative for at least 13 independent experiments.
Supplementary Video	3	Supplementary_video_3.avi	Localization of the dimer's mRNA at condensates. mRNAs coding for the dimer building block localize at condensates in yeast cells. The video is representative for at least three independent experiments.
Supplementary Video	4	Supplementary_video_4.avi	Localization of GB1 mRNA. mRNAs coding for GB1, a protein that does not bind condensates, do co-localize with condensates. The video is representative for at least three independent experiments.
Supplementary Video	5	Supplementary_video_5.avi	C-terminal variant of the binding domain. mRNAs do not localize at condensates when the binding domain is encoded at the C-terminus of the dimer. The video is representative for at least three independent experiments.
Supplementary Video	6	Supplementary_video_6.	Puromycin.

		avi	mRNAs detach from condensates in yeast cells treated with puromycin. The video is representative for at least three independent experiments.
Supplementary Video	7	Supplementary_video_7.avi	Puromycin + CHX. mRNAs remain localized at condensates in yeast cells treated with puromycin and cycloheximide. The video is representative for at least three independent experiments.

3. Source Data

10

11

Parent Figure or Table	Filename	Data description
	This should be the name the file is saved as when it is uploaded to our system, and should include the file extension. i.e.: <i>Smith_SourceData_Fig1.xls</i> , or <i>Smith_Unmodified_Gels_Fig1.pdf</i>	i.e.: Unprocessed Western Blots and/or gels, Statistical Source Data, etc.
Source Data Fig. 2g	Figure_2G_Source_Data.xlsx	Data for the phase diagrams
Source Data Fig. 3a	Figure_3A_Source_Data.xlsx	Data for the phase diagrams
Source Data Extended Data Fig. 5	Ext_Data_Figure_5_Source_Data.xlsx	Data for the phase diagrams
Source Data Extended Data Fig. 6	Ext_Data_Figure_6_Source_Data.xlsx	Data for the phase diagrams

12

13

14

15 Designer protein assemblies with tunable phase diagrams in living cells

16

17 Meta Heidenreich^{1*}, Joseph M. Georgeson^{1*}, Emanuele Locatelli⁷, Lorenzo Rovigatti^{5,6,§}, Saroj Kumar
18 Nandi^{2,4}, Avital Steinberg¹, Yotam Nadav¹, Eyal Shimoni³, Samuel A. Safran^{2,§}, Jonathan P. K. Doye^{5,§},
19 Emmanuel D. Levy^{1,§}

20

21 1 Department of Structural Biology, Weizmann Institute of Science, Rehovot, Israel.

22 2 Department of Chemical and Biological Physics, Weizmann Institute of Science, Rehovot, Israel.

23 3 Department of Chemical Research Support, Weizmann Institute of Science, Rehovot, Israel

24 4 TIFR Centre for Interdisciplinary Sciences, Tata Institute of Fundamental Research, Hyderabad, India

25 5 Physical & Theoretical Chemistry Laboratory, Department of Chemistry, University of Oxford, Oxford, UK

26 6 Department of Physics, Sapienza Università di Roma, Rome, Italy

27 7 Faculty of Physics, University of Vienna, Vienna, Austria

28 * These authors contributed equally to this work

29 § Authors for correspondence

30 Emails (ORCID):

31 lorenzo.rovigatti@gmail.com (0000-0001-5017-2829),

32 sam.safran@weizmann.ac.il (0000-0002-0798-1492),

33 jonathan.doye@chem.ox.ac.uk (0000-0002-2226-9524),

34 emmanuel.Levy@weizmann.ac.il (0000-0001-8959-7365)

35

36 Document statistics

37 Main text: 3637 words

38 Methods: 1849 words

39 Figures: 4

40 Tables: 1

41 Extended Data Figures: 7

42 Supplementary Figures: 5

43 Supplementary Tables: 3

44 Supplementary Note: 1

45 Supplementary Excel (Data Source): 2

46 Supplementary Videos: 7

47

48 Abstract

49 Proteins self-organization is a hallmark of biological systems. Physico-chemical principles governing
50 protein-protein interactions have long been known. However, the principles by which such nanoscale
51 interactions generate diverse phenotypes of mesoscale assemblies, including phase-separated
52 compartments, remain challenging to characterize. To illuminate such principles, we create a system of
53 two proteins designed to interact and form mesh-like assemblies. We devise a novel strategy to map high-
54 resolution phase diagrams in living cells, which provide self-assembly signatures of this system. The
55 structural modularity of the two protein components allows straightforward modification of their
56 molecular properties, enabling us to characterize how interaction affinity impacts the phase diagram and
57 material state of the assemblies *in vivo*. The phase diagrams and their dependence on interaction affinity
58 were captured by theory and simulations, including out-of-equilibrium effects seen in growing cells.
59 Finally, we find that cotranslational protein binding suffices to recruit an mRNA to the designed micron-
60 scale structures.

61 Introduction

62 The self-organization and proper function of complex systems involve elaborate spatiotemporal
63 coordination of their constituent elements. Cells organize their contents into organelles, which have been
64 classically viewed as membrane-bound structures. However, in recent years, an increasing number of
65 studies describe fundamentally different types of organelles that form by phase separation and are not
66 membrane-bound¹. These organelles, also called biomolecular condensates² are associated with diverse

67 functions^{1,3,4}, ranging from pre-mRNA processing⁵ and translation regulation⁶ to signalling⁷, or to the
68 formation of eye lenses⁸. The increasingly frequent discovery of such organelles reflects that we are only
69 beginning to grasp the complexity underlying the proteome's spatial organization and begs for a
70 molecular understanding of the process of phase separation in living cells.

71

72 In phase separation, thousands of copies of identical molecules cluster and interact together, implying
73 that small changes in molecular properties of components, e.g., by mutation, can propagate and
74 dramatically impact macroscopic phenotypes of assembly⁹. For example, mutations increasing the
75 viscosity of FUS and Huntington exon 1 condensates have been associated with debilitating diseases such
76 as amyotrophic lateral sclerosis (ALS), frontotemporal dementia (FTD)^{10,11}, and Huntington¹². However,
77 there is little understanding of how these mutations act at the molecular level to change the phase
78 behavior and viscosity of condensates. In order to bridge this gap, it is crucial to connect biophysical
79 properties of proteins to mesoscale phenotypes of their assembly inside of living cells.

80

81 Establishing such a nanoscale-mesoscale connection with natural condensates is hardly possible due to
82 their compositional and regulatory complexity. Creating synthetic condensates offers a powerful
83 alternative, as both the structure and biophysical properties of the components can be known by design.
84 Furthermore, if the proteins employed are orthogonal to the living system, no active cellular regulation is
85 expected to take place. Previous work based on synthetic proteins showed that increasing multivalence of
86 the components promotes their phase separation^{13,14}, and revealed how distinct client proteins can be
87 differentially recruited to condensates². However, detailed molecular modeling of these systems is
88 difficult, since the interaction affinity between individual components was fixed¹³ or unknown¹⁴, and the
89 contribution of intra- versus inter-molecular interactions was also unknown. Moreover, in such systems,
90 interaction affinities and the balance of inter- versus intramolecular interactions cannot be tuned
91 independently from one another. These limitations prompted us to design a synthetic system providing
92 control over these nanoscale properties.

93

94 Here we introduce this minimal system, which consists of two protein components. We show that this
95 system allows the direct visualization of its phase diagram in living cells. By mapping the phase diagram
96 of point mutants modulating the binding affinity between the two components, we demonstrate that
97 increasing affinity enhances phase separation *in vivo*, until the system becomes kinetically trapped at very
98 high affinities. Finally, we applied our system to interrogate biological mechanisms of self-assembly. We
99 found that one of the system's components binds co-translationally to the condensate, indicating that co-
100 translational protein binding of a nascent chain can suffice to localize its mRNA.

101 **Results**

102 ***A synthetic two-protein system that phase separates***

103 A quantitative and detailed molecular understanding of biophysical and biological mechanisms of
104 mesoscale self-assembly requires a system where all parameters, namely the components, their structure,
105 and their physical interactions, are known. To this aim, we developed a synthetic system in which these
106 properties are controlled by design. The system comprises two protein components that interact with
107 affinities tunable by point mutation. Each component is designed in a modular fashion and consists of
108 three structured domains linked by short flexible linkers. As we know from previous work that
109 multivalence is a critical property of molecules undergoing phase separation^{13,15}, both components are

110 multivalent. The first component contains a homo-dimerization domain, a red fluorescent protein (RFP),
111 and the protein Im2. The second component contains a homo-tetramerization domain, a yellow
112 fluorescent protein (YFP), and the protein E9, which interacts specifically with Im2 ([Figure 1a](#), Methods,
113 Supplementary Table 1). Importantly, unlike in other synthetic systems^{13,14}, intramolecular interactions
114 are restricted by an incompatibility between the distances separating the termini to which interaction
115 domains are fused, equal to 18 nm on the dimer and only 4 nm on the tetramer ([Figure 1a, b](#)).
116

117 We co-expressed the dimer and tetramer components in yeast cells. Using fluorescence microscopy, we
118 observed the formation of sub-micron to micron-scale punctate assemblies where the tetramer and dimer
119 co-localized ([Figure 1c](#), Video 1), suggesting that the system undergoes phase separation and forms
120 condensates. The assembly of this system was dependent on the specific interaction between E9 and Im2,
121 as condensates were neither observed when co-expressing the tetramer with a dimer lacking the Im2
122 domain ([Figure 1d](#)) nor were they observed in haploid cells that expressed only one of the components
123 (Extended Data Figure 1). The assemblies were not membrane-bound, as visualized by electron
124 microscopy (Extended Data Figure 2).

125 ***Revealing phase diagrams in vivo at high-resolution***

126 The physical origin of phase separation of molecules in solution is the attraction between them, which, in
127 the appropriate range of concentration and interaction-strength, dominates the entropy of mixing. In our
128 system, dimers mediate indirect tetramer-tetramer attraction. At equilibrium, this attraction gives rise to
129 two coexisting phases with equal chemical potential and osmotic pressure: a dense phase where
130 tetramers and dimers show high concentrations, high enthalpy, and low entropy, and a dilute phase with
131 lower concentrations of dimers and tetramers, lower enthalpy, and higher entropy.
132

133 In cells, the dense phase corresponds to the condensate and the dilute phase consists of freely diffusing
134 components in the cytoplasm ([Figure 2a](#)). The conditions under which phase separation occurs at
135 equilibrium are described by its phase diagram, with the binodal defining phase boundaries. We
136 developed a lattice model ([Figure 2b](#), Methods) to predict the phase diagram of our system as a function
137 of dimer and tetramer concentrations ([Figure 2c](#)). Concentrations outside of the binodal do not drive
138 phase separation, either because they are too low relative to the interaction affinity ([Figure 2d](#)), or
139 because an imbalance in the components' stoichiometry inhibits the propagation of their interactions in
140 multicomponent systems^{13,15-20} ([Figure 2e](#)).
141

142 Interestingly, cells without condensates have not undergone phase separation and should fall outside of
143 the binodal. Thus, the region of concentrations that is absent in these cells should reveal the phase
144 boundary of this system ([Figure 2f](#)). Such an approach offers the unique opportunity to map a high-
145 resolution phase diagram *in vivo*, because the phase-space can be defined along two continuous
146 coordinates corresponding to the concentrations of each component. Unlike temperature or pressure,
147 protein concentration can be tuned over several orders of magnitude and can be measured readily from
148 fluorescence intensity across thousands of single cells.
149

150 To characterize such a phase diagram, we created yeast strains co-expressing the dimer and tetramer
151 components independently, such that each cell sampled a different point of the phase space. We imaged
152 thousands of single cells and estimated the components' concentrations from fluorescence intensity
153 (Supplementary Figure 1), excluding cells containing a condensate to ascertain reliable concentration

154 measurements ([Figure 2f](#), Methods). As predicted, the density distribution of cells revealed the phase
155 boundary of the system ([Figure 2g](#)).
156

157 ***Modeling the phase diagram measured in vivo***

158 The phase boundary appears as an area where cell density approaches zero. The scarcity of cells sampling
159 concentrations beyond 10 μM prevented visualizing closed boundaries, giving rise to a half-ellipsoid. We
160 modeled the expected boundaries using a minimal lattice model, where tetramers occupy the vertices,
161 dimers occupy the bonds, and solvent molecules can occupy either the vertices or bonds. ([Figure 2b,c](#) and
162 Methods).
163

164 Furthermore, we generated phase diagrams using thermodynamic perturbation theory developed for
165 patchy particles matching the geometry of our proteins (Supplementary Figure 2, Supplementary Note).
166 Both methodological approaches recapitulated our observations: the half-ellipsoid aligns along the
167 diagonal where the stoichiometry of both components' binding sites is equal (Figure 2g, Extended Data
168 Figure 3). Indeed, a balanced stoichiometry gives rise to a lower energy assembly, where enthalpy is
169 maximal with all binding sites satisfied, thus favoring phase separation. As stoichiometries become
170 unbalanced (e.g., 1:10 or 10:1), the component present in excess saturates all binding sites of its partner,
171 which inhibits propagation of interactions and phase separation ([Figure 2e](#)).
172

173 ***Tuning phase diagram and viscosity by affinity***

174 The nature of the interaction domains used in this system allows both lowering and increasing the affinity
175 by single point mutations²¹ described in [Table 1](#). We initially investigated four new variants for the dimer,
176 which contained point mutations modulating the dissociation constant between Im2 and E9 domains
177 across five orders of magnitude, from 10^{-11} to 10^{-6} M.
178

179 We imaged yeast cells co-expressing the tetramer with the new dimer variants, and generated their *in*
180 *vivo* phase diagrams ([Figure 3](#) and Extended Data Figure 5). Mutants interacting with an affinity lower
181 than that of the wild-type domains showed a shift in their phase diagram. The half-ellipsoid underwent a
182 translation along the diagonal, towards higher concentrations. Such a translation was expected, as lower
183 interaction affinities require higher concentrations for binding. The same effect is reproduced with the
184 two theoretical approaches we put forward (Extended Data Figure 3). Interestingly, the mutant with an
185 affinity of 4.8×10^{-11} M (higher affinity than the wild type) revealed a complex behavior: the minimal
186 concentration of tetramer required for phase separation increased, as reflected in the upward shift of the
187 phase boundary (yellow region, [Figure 3a](#)).
188

189 This upward shift led us to examine the diffusion dynamics of components within condensates. Fast
190 diffusion requires components to be unbound, and their probability to exist in the unbound state is
191 inversely proportional to their interaction affinity (Supplementary Note). Thus, we expect high-affinity
192 interactions to yield condensates with slow diffusion dynamics, whereas lower affinities should yield
193 faster diffusion dynamics. To test this hypothesis, we measured fluorescence recovery after
194 photobleaching (FRAP) of the condensates. Considering low, medium and high-affinity interactions ($2.1 \times$
195 10^{-6} M, 2.8×10^{-7} M, and 4.8×10^{-11} M), the mean fluorescence recovery after 25 seconds reached $65 \pm 4\%$,
196 $56 \pm 4\%$ and $15 \pm 2\%$, respectively ([Figure 3b and c](#), Extended Data Figure 5, Video 2). Individual traces

197 show pronounced variability in the recovery profiles, especially at low affinities, which might reflect
198 differences in condensate density as well as differences in the fraction of bonded components
199 (Supplementary Figure 3). On average, however, higher interaction affinity led to slower diffusion of
200 components, consistent with the effective viscosity of the condensates being controlled by interaction
201 affinity. Importantly, the slower recovery of the D33L Im2 mutant implies that it does interact with a
202 higher affinity than wild-type Im2, which is in conflict with the observed shrinkage in phase boundaries
203 (yellow region, [Figure 3a](#)). This apparent contradiction might originate in kinetics. At high affinity, the
204 kinetics of unbinding events is very slow, which can trap the system in states where both components
205 have a non-optimal distribution of bonds in the network. Nonetheless, dimers need to be completely
206 bonded to mediate cluster growth, whereas tetramers require only two out of four bonds to mediate such
207 growth. Consequently, misplaced bonds in a tetramer-poor system would hinder the formation of a
208 network more than they would in a tetramer-rich system. This idea led us to compare the regions where
209 phase separation occurs in equilibrium versus out-of-equilibrium molecular dynamics simulations of
210 patchy particles (Extended Data Figure 4a). These simulations confirmed the picture sketched above by
211 revealing a shift in the lower branch of the phase diagram, while the upper branch remained essentially
212 unmoved (Extended Data Figure 4b, Supplementary Figure 4, Supplementary Figure 5, Supplementary
213 Note).

214
215 To further corroborate that kinetic trapping inhibits phase separation we created a yeast strain where
216 components interact with an even higher affinity (3.4×10^{-13} M, Table 1). This mutant showed a more
217 pronounced upward shift of the lower branch, further supporting that the system gets kinetically trapped
218 at very high affinities (Extended Data Figure 6). Moreover, to narrow the affinity range at which kinetic
219 trapping becomes visible, we created three additional variations of the system where the dimer and
220 tetramer interact with intermediate affinities (3.3×10^{-9} M, 2.6×10^{-9} M, 1.9×10^{-10} M, Table 1). We
221 measured *in vivo* phase diagrams for these new variants, and observed that the upward shift appears at
222 an affinity of 1.9×10^{-10} M, and only becomes pronounced at 4.8×10^{-11} M (Extended Data Figure 6).

223 ***Cotranslational binding suffices to localize mRNA***

224
225 The spatial organization of translation is achieved by mRNA trafficking and localization²². Interestingly,
226 mRNA localization could be achieved by the proteins being synthesized, if they can bind localized
227 partners cotranslationally. This mechanism had, in fact, been suggested to mediate the localization of
228 mRNAs encoding myosin heavy chain in developing cultured skeletal muscles²³. However, considering a
229 biological system, it is hard to address whether cotranslational binding of a nascent polypeptide chain can
230 suffice to localize its encoding mRNA, because other mechanisms could be involved.

231
232 Additionally, cotranslational binding can be hindered by numerous factors. Indeed, polysomes diffuse
233 slower than globular proteins due to their large size, so a nascent chain may not reach a particular
234 localization within the time of translation. In parallel, the interacting region of the nascent chain must be
235 exposed at the surface of the ribosome for a sufficiently long time to mediate binding with the target. As a
236 result, and as observed for cotranslational assembly of protein complexes²⁴⁻²⁶, the N- versus C- terminal
237 positioning of the interaction region may play an important role. These limiting factors beg the question:
238 can cotranslational binding suffice to determine the localization of a polysome?

239
240 Uniquely, our synthetic system makes it possible to address this question directly because we know that
241 its components have neither evolved to bind their own mRNA, nor RNAs in general. We fused the mRNA
242 encoding the dimer component to a sequence enabling its tracking in live cells²⁷. In these experiments, we

243 used a tetramer component fused to a blue fluorescent reporter, so that green fluorescence was solely
244 reporting on mRNA localization. Live cell imaging revealed that mRNAs diffused throughout the cell and
245 attached to the condensate when they encountered it. Surprisingly, multiple mRNAs could co-localize and
246 appeared to nucleate the formation of the condensate (Figure 4a and d, Video 3). In contrast, an mRNA
247 coding for a protein that does not bind to the condensate did not co-localize with it (Figure 4b,d, Video 4).
248 As an additional control, we changed the position of the binding domain of the dimer from N- to C-
249 terminus. In this new construct, the binding domain is released from the ribosome right after its
250 synthesis. Therefore, this construct is not expected to mediate cotranslational assembly^{24,25} and its mRNA
251 should not localize to the condensate. In agreement with this prediction, we did not observe recruitment
252 of the dimer's mRNA to the condensate when the binding domain was encoded in its C-terminus (Figure
253 4c and d, Video 5). This result also implies that dimerization is not occurring co-translationally, possibly
254 because the dimer interface involves the C-terminus that is not exposed at the surface of the ribosome for
255 a sufficiently long time.

256 To provide a quantitative description of these live-cell imaging observations, we measured the
257 distribution of distances between the center of foci corresponding to mRNAs (green) and condensates
258 (red, see methods). As expected, the mRNAs of dimers harboring an N- terminal binding region co-
259 localized with condensates (mean distance of $0.48 \pm 0.19 \mu\text{m}$), whereas the mRNAs of dimers harboring a
260 C-terminal binding domain showed a mean distance of $1.85 \pm 1.49 \mu\text{m}$ and encompassed values as large
261 as the diameter of a yeast cell. This latter distance distribution is not significantly different from that of a
262 negative control, i.e., an mRNA encoding a protein that does not bind to the condensate (mean distance of
263 $1.83 \pm 1.29 \mu\text{m}$).

264
265 To ascertain that recruitment of the mRNA to the condensate is translation dependent, we employed
266 puromycin, a drug that dissociates translating ribosomes from mRNA. Treatment of cells with puromycin
267 released the dimers' mRNA from the condensate within minutes (Figure 4e, Video 6, Extended Data
268 Figure 7). Interestingly, cycloheximide prevents puromycin mediated dissociation of ribosomes from
269 their mRNA²⁸, providing another means to test the translation dependence of mRNA localization to the
270 condensate. When treated simultaneously with puromycin and cycloheximide, mRNAs maintained their
271 co-localization with condensates (Figure 4f, Video 7).

272
273 To gain a quantitative view of these experiments, we followed cells exhibiting co-localization between
274 mRNA and condensate before treatment, and recorded how many of these cells exhibited complete
275 detachment of the mRNA after treatment with puromycin alone, or puromycin together with
276 cycloheximide (Extended Data Figure 7). While puromycin treatment led to complete detachment of
277 mRNA(s) in 88% of cases, the addition of cycloheximide cancelled this effect as complete detachment
278 occurred in only 6% of cases (Figure 4g). Together, these results point to cotranslational binding of a
279 nascent chain as a mechanism that can drive the localization of its encoding mRNA.

280

281 Discussion and conclusions

282 We designed and characterized a synthetic minimal system to study *in vivo* phase separation from first
283 principles. Notably, the folded nature of interaction domains of our system, together with the defined
284 geometry of oligomerization domains provide unprecedented control over the biophysical and structural
285 properties of the components. At the same time, we introduce a novel strategy using single cells as
286 individual "test-tubes" to map high-resolution phase diagrams *in vivo*. Combined, these properties create

287 a powerful experimental system to relate nanoscale to mesoscale phenotypes of self-assembly from first
288 principles. We explore this relationship by characterizing how mutations changing the interaction affinity
289 between the two components impact the phase behavior and material state of the condensates they form.
290 Interestingly, numerous additional parameters such as linker properties, electrostatics, or valence could
291 be tuned independently from one another, and their impact on phase separation characterized and
292 modeled in the same way.

293
294 The ability to dissect how individual parameters impact phase separation is essential for understanding
295 biological condensates, because they involve several layers of complexity. At a biophysical level, intricate
296 dependencies can exist between three parameters: affinity, multivalency, and concentration. For instance,
297 an increased valence will lead to an increased apparent affinity, which in turn lowers the minimal
298 concentration for phase separation^{13,29}. At the same time, the apparent valence of a molecule with
299 multiple self-interacting regions can change with concentration, because inter- and intra-molecular
300 binding events compete³⁰⁻³². Furthermore, at a biological level, the identity of the components, the way in
301 which they interact, and how they are regulated, is often unknown.

302
303 Our system helps address these layers of complexity: biophysically, the impact of intermolecular
304 interaction affinity we observed is also expected in biological systems. For example, increased salt
305 concentration inhibits phase-separation and decreases the viscosity of LAF-1 condensates. These results
306 are consistent with our observations, whereby salt would decrease the effective affinity of LAF-1 for itself.
307 Conversely, mutations in the low complexity domain of TIA1 were shown to enhance its phase separation
308 and decrease its mobility in condensates³³. In line with our results, these observations indicate a
309 strengthening of intermolecular interactions in TIA1 condensates. At a biological level, the oval-shaped
310 phase boundaries imply that increasing the expression of components *in vivo* can inform on whether a
311 single or multiple components are required for phase separation. Indeed, in a multi-component system,
312 increasing the concentration of one component relative to the other dissolves the dense phase at
313 equilibrium. However, if a single component is sufficient, increasing its concentration will result in a
314 larger dense phase. Theoretically, this prediction applies to condensates involving any type of molecule
315 (e.g., folded proteins, disordered regions, RNAs, or a combination of these). For example, NPM1 and
316 poly(PR) peptides interact and phase separate together. Similar to our system, very high concentrations
317 of poly(PR) lead to the droplet dissolution *in vitro*³⁴. Such behavior has also been described for a system
318 involving RNA interacting with PR-rich peptides³⁵.

319
320 Finally, our synthetic system can serve to identify novel synergisms between protein self-assembly and
321 cellular processes. Recent works have revealed cotranslational assembly of complexes as a widespread
322 mechanism^{24,36} actively shaped by evolution^{25,37}. Our results now suggest that cotranslational binding of a
323 nascent chain can be sufficient to localize mRNAs in cells. Interestingly, several mechanisms for mediating
324 interactions between RNA and proteins in condensates are known^{38,39}, and the results presented here
325 suggest cotranslational assembly as a new such mechanism. The design of mesoscale synthetic protein
326 assemblies is becoming increasingly powerful to create new materials⁴⁰⁻⁴² and functions^{43,44}. Moreover, as
327 we are only beginning to grasp the complexity of proteome self-organization, new approaches are needed
328 for characterizing and understanding mesoscale properties of protein self-assembly in cells^{19,20,32,45-50}. In
329 this context, our synthetic system constitutes a powerful tool to interrogate biological mechanisms of
330 protein assembly. In the future, it may serve to evaluate and calibrate physical models of self-assembly *in*
331 *vivo*, and form a basis for developing new biomaterials and scaffolds in living cells.

332 **Acknowledgments**

333 We thank J. Gerst and R.R. Nair (Weizmann Institute, IL) for sharing plasmids of the MS2 system, S.
334 Schwartz (Weizmann Institute, IL) for the bRA89 plasmid, F. Sciortino and H. Hofmann for helpful
335 discussions and suggestions, and H. Greenblatt for help with computer systems. E.D.L. acknowledges
336 support by the Israel Science Foundation (1452/18), by the European Research Council (ERC) under the
337 European Union's Horizon 2020 research and innovation programme (grant agreement No. 819318), by
338 the HFSP Career Development Award (award no. CDA00077/2015), by a research grant from A.-M.
339 Boucher, by research grants from the Estelle Funk Foundation, the Estate of Fannie Sherr, the Estate of
340 Albert Deligher, the Merle S. Cahn Foundation, Mrs. Mildred S. Gosden, the Estate of Elizabeth Wachsman,
341 the Arnold Bortman Family Foundation. E.D.L. is incumbent of the Recanati Career Development Chair of
342 Cancer Research. L.R. acknowledges support from the European Commission (Marie Skłodowska-Curie
343 Fellowship No. 702298-DELTAS). S.A.S. thanks the BSF and the ISF program and acknowledges the
344 historical generosity of the Perlmann family foundation. S.K.N. acknowledges support from the Koshland
345 foundation.

346 **Authors contributions**

347 M.H., J.M.G. and E.D.L. designed the research and synthetic protein system -- M.H., J.M.G. performed the
348 experiments with help from Y.N. -- E.L., L.R. and J.K.P.D developed the theoretical framework for modeling
349 the system based on patchy particles -- S.N. and S.S. developed the theoretical framework for modeling
350 the system based on a lattice model -- A.S. wrote the image analysis scripts; E.S. carried out electron
351 microscopy experiments -- M.H. and E.D.L. wrote the manuscript with input from all authors.

353 **Competing Interests**

354
355 The authors declare no competing interests
356

357 **References**

- 358 1. Hyman, A. A., Weber, C. A. & Julicher, F. Liquid-liquid phase separation in biology. *Annu. Rev. Cell*
359 *Dev. Biol.* **30**, 39–58 (2014).
- 360 2. Banani, S. F. *et al.* Compositional Control of Phase-Separated Cellular Bodies. *Cell* **166**, 651–663
361 (2016).
- 362 3. Holehouse, A. S. & Pappu, R. V. Functional Implications of Intracellular Phase Transitions.
363 *Biochemistry* **57**, 2415–2423 (2018).
- 364 4. Banani, S. F., Lee, H. O., Hyman, A. A. & Rosen, M. K. Biomolecular condensates: organizers of
365 cellular biochemistry. *Nat. Rev. Mol. Cell Biol.* **18**, 285–298 (2017).
- 366 5. Tatomer, D. C. *et al.* Concentrating pre-mRNA processing factors in the histone locus body
367 facilitates efficient histone mRNA biogenesis. *J. Cell Biol.* **213**, 557–570 (2016).
- 368 6. Buchan, J. R. & Parker, R. Eukaryotic stress granules: the ins and outs of translation. *Mol. Cell* **36**,
369 932–941 (2009).
- 370 7. Su, X. *et al.* Phase separation of signaling molecules promotes T cell receptor signal transduction.
371 *Science* **352**, 595–599 (2016).
- 372 8. Cai, J., Townsend, J. P., Dodson, T. C., Heiney, P. A. & Sweeney, A. M. Eye patches: Protein assembly
373 of index-gradient squid lenses. *Science* **357**, 564–569 (2017).
- 374 9. Garcia-Seisdedos, H., Empereur-Mot, C., Elad, N. & Levy, E. D. Proteins evolve on the edge of

- 375 supramolecular self-assembly. *Nature* **548**, 244–247 (2017).
- 376 10. Murakami, T. *et al.* ALS/FTD Mutation-Induced Phase Transition of FUS Liquid Droplets and
377 Reversible Hydrogels into Irreversible Hydrogels Impairs RNP Granule Function. *Neuron* **88**, 678–690
378 (2015).
- 379 11. Patel, A. *et al.* A Liquid-to-Solid Phase Transition of the ALS Protein FUS Accelerated by Disease
380 Mutation. *Cell* **162**, 1066–1077 (2015).
- 381 12. Peskett, T. R. *et al.* A Liquid to Solid Phase Transition Underlying Pathological Huntingtin Exon1
382 Aggregation. *Mol. Cell* **70**, 588–601.e6 (2018).
- 383 13. Li, P. *et al.* Phase transitions in the assembly of multivalent signalling proteins. *Nature* **483**, 336–
384 340 (2012).
- 385 14. Bracha, D. *et al.* Mapping Local and Global Liquid Phase Behavior in Living Cells Using Photo-
386 Oligomerizable Seeds. *Cell* **176**, 407 (2019).
- 387 15. Flory, P. J. *Principles of Polymer Chemistry*. (Cornell University Press, 1953).
- 388 16. Smallenburg, F., Leibler, L. & Sciortino, F. Patchy particle model for vitrimers. *Phys. Rev. Lett.* **111**,
389 188002 (2013).
- 390 17. Bianchi, E., Largo, J., Tartaglia, P., Zaccarelli, E. & Sciortino, F. Phase diagram of patchy colloids:
391 Towards empty liquids. *Phys. Rev. Lett.* **97**, 168301 (2006).
- 392 18. Falkenberg, C. V., Blinov, M. L. & Loew, L. M. Pleomorphic ensembles: formation of large clusters
393 composed of weakly interacting multivalent molecules. *Biophys. J.* **105**, 2451–2460 (2013).
- 394 19. Jacobs, W. M. & Frenkel, D. Phase Transitions in Biological Systems with Many Components.
395 *Biophys. J.* **112**, 683–691 (2017).
- 396 20. Sanders, D. W. *et al.* Competing Protein-RNA Interaction Networks Control Multiphase
397 Intracellular Organization. *Cell* **181**, 306–324.e28 (2020).
- 398 21. Li, W. *et al.* Dual recognition and the role of specificity-determining residues in colicin E9 DNase-
399 immunity protein interactions. *Biochemistry* **37**, 11771–11779 (1998).
- 400 22. Buxbaum, A. R., Haimovich, G. & Singer, R. H. In the right place at the right time: visualizing and
401 understanding mRNA localization. *Nat. Rev. Mol. Cell Biol.* **16**, 95–109 (2015).
- 402 23. Isaacs, W. B. & Fulton, A. B. Cotranslational assembly of myosin heavy chain in developing
403 cultured skeletal muscle. *Proc. Natl. Acad. Sci. U. S. A.* **84**, 6174–6178 (1987).
- 404 24. Shiber, A. *et al.* Cotranslational assembly of protein complexes in eukaryotes revealed by
405 ribosome profiling. *Nature* **561**, 268–272 (2018).
- 406 25. Natan, E. *et al.* Cotranslational protein assembly imposes evolutionary constraints on homomeric
407 proteins. *Nat. Struct. Mol. Biol.* **25**, 279–288 (2018).
- 408 26. Kramer, G., Shiber, A. & Bukau, B. Mechanisms of Cotranslational Maturation of Newly Synthesized
409 Proteins. *Annu. Rev. Biochem.* **88**, 337–364 (2019).
- 410 27. Haim-Vilmovsky, L. & Gerst, J. E. m-TAG: a PCR-based genomic integration method to visualize the
411 localization of specific endogenous mRNAs in vivo in yeast. *Nat. Protoc.* **4**, 1274–1284 (2009).
- 412 28. Lui, J. *et al.* Granules Harboring Translationally Active mRNAs Provide a Platform for P-Body
413 Formation following Stress. *Cell Reports* vol. 9 944–954 (2014).
- 414 29. Shin, Y. *et al.* Spatiotemporal Control of Intracellular Phase Transitions Using Light-Activated
415 optoDroplets. *Cell* vol. 168 159–171.e14 (2017).
- 416 30. Dignon, G. L., Zheng, W., Best, R. B., Kim, Y. C. & Mittal, J. Relation between single-molecule
417 properties and phase behavior of intrinsically disordered proteins. *Proc. Natl. Acad. Sci. U. S. A.* **115**, 9929–
418 9934 (2018).
- 419 31. Dignon, G. L., Zheng, W. & Mittal, J. Simulation methods for liquid–liquid phase separation of
420 disordered proteins. *Curr. Opin. Chem. Eng.* **23**, 92–98 (2019).
- 421 32. Yang, P. *et al.* G3BP1 Is a Tunable Switch that Triggers Phase Separation to Assemble Stress
422 Granules. *Cell* **181**, 325–345.e28 (2020).
- 423 33. Mackenzie, I. R. *et al.* TIA1 Mutations in Amyotrophic Lateral Sclerosis and Frontotemporal
424 Dementia Promote Phase Separation and Alter Stress Granule Dynamics. *Neuron* **95**, 808–816.e9 (2017).
- 425 34. White, M. R. *et al.* C9orf72 Poly(PR) Dipeptide Repeats Disturb Biomolecular Phase Separation and
426 Disrupt Nucleolar Function. *Mol. Cell* **74**, 713–728.e6 (2019).
- 427 35. Banerjee, P. R., Milin, A. N., Moosa, M. M., Onuchic, P. L. & Deniz, A. A. Reentrant Phase Transition

- 428 Drives Dynamic Substructure Formation in Ribonucleoprotein Droplets. *Angew. Chem. Int. Ed Engl.* **56**,
429 11354–11359 (2017).
- 430 36. Duncan, C. D. S. & Mata, J. Widespread cotranslational formation of protein complexes. *PLoS Genet.*
431 **7**, e1002398 (2011).
- 432 37. Shieh, Y.-W. *et al.* Operon structure and cotranslational subunit association direct protein
433 assembly in bacteria. *Science* **350**, 678–680 (2015).
- 434 38. Langdon, E. M. & Gladfelter, A. S. A New Lens for RNA Localization: Liquid-Liquid Phase
435 Separation. *Annu. Rev. Microbiol.* **72**, 255–271 (2018).
- 436 39. Boeynaems, S. *et al.* Protein Phase Separation: A New Phase in Cell Biology. *Trends Cell Biol.* **28**,
437 420–435 (2018).
- 438 40. Garcia-Seisdedos, H., Villegas, J. A. & Levy, E. D. Infinite Assembly of Folded Proteins in Evolution,
439 Disease, and Engineering. *Angew. Chem. Int. Ed Engl.* **58**, 5514–5531 (2019).
- 440 41. Shen, H. *et al.* De novo design of self-assembling helical protein filaments. *Science* **362**, 705–709
441 (2018).
- 442 42. Abe, S. *et al.* Crystal Engineering of Self-Assembled Porous Protein Materials in Living Cells. *ACS*
443 *Nano* **11**, 2410–2419 (2017).
- 444 43. Reinkemeier, C. D., Girona, G. E. & Lemke, E. A. Designer membraneless organelles enable codon
445 reassignment of selected mRNAs in eukaryotes. *Science* **363**, (2019).
- 446 44. Lee, M. J. *et al.* Engineered synthetic scaffolds for organizing proteins within the bacterial
447 cytoplasm. *Nat. Chem. Biol.* **14**, 142–147 (2018).
- 448 45. Delarue, M. *et al.* mTORC1 Controls Phase Separation and the Biophysical Properties of the
449 Cytoplasm by Tuning Crowding. *Cell* **174**, 338–349.e20 (2018).
- 450 46. Chavent, M. *et al.* How nanoscale protein interactions determine the mesoscale dynamic
451 organisation of bacterial outer membrane proteins. *Nat. Commun.* **9**, 2846 (2018).
- 452 47. Alberti, S., Gladfelter, A. & Mittag, T. Considerations and Challenges in Studying Liquid-Liquid
453 Phase Separation and Biomolecular Condensates. *Cell* **176**, 419–434 (2019).
- 454 48. Wang, J. *et al.* A Molecular Grammar Governing the Driving Forces for Phase Separation of Prion-
455 like RNA Binding Proteins. *Cell* **174**, 688–699.e16 (2018).
- 456 49. Choi, J.-M., Dar, F. & Pappu, R. V. LASSI: A lattice model for simulating phase transitions of
457 multivalent proteins. *PLoS Comput. Biol.* **15**, e1007028 (2019).
- 458 50. Panasenko, O. O. *et al.* Co-translational assembly of proteasome subunits in NOT1-containing
459 assemblysomes. *Nat. Struct. Mol. Biol.* **26**, 110–120 (2019).
- 460
461

462 **Figure Legends**

463

464 **Figure 1. A synthetic system for controlled phase separation in living cells.** **a.** The components, each encoded
465 in one ORF, consist of three domains connected by flexible linkers: An interaction domain, an oligomerization
466 domain, and a fluorescent protein. The Colicin (E9, cyan) and Immunity (Im2, orange) proteins serve as interaction
467 modules, where affinity is controllable by mutation. A dimer and tetramer of known structure (Supplementary Table
468 1) served as divalent and tetravalent scaffolds. We fused Im2 and a red fluorescent protein (RFP) to the dimer, and
469 E9 and a yellow fluorescent protein (YFP) to the tetrameric scaffold. **b.** Illustrative structure of a dimer interacting
470 with two tetramers, and cartoon representation underneath. **c.** The system undergoes self-assembly and forms
471 punctate structures in living yeast cells. Scalebar: 10 μm **d.** In the absence of the Im2 interaction module, no
472 punctate structure is formed. These results were independently replicated three times.

473

474 **Figure 2. Characterizing phase diagrams in living cells.** **a.** The phase diagram describes when the system phase
475 separates in a given parameter space, here defined by the dimer and tetramer concentrations. Concentrations within
476 the binodal (yellow dotted line) are not stable, as for the crossed-out cell, leading to phase separation into a dilute
477 and a dense phase (condensate). **b.** A lattice model captures the essence of phase separation, whereby the chemical
478 potential of the dimer and tetramer exhibit two minima, the first with high entropy and low enthalpy (dilute phase),
479 and the second with low entropy and high enthalpy from the bonding energy (dense phase). **c.** Based on this lattice
480 model we derive a phase diagram showing the binodal, two critical points and ties lines. **d.** Cells without condensate

481 may have concentrations of both components that are too low. **e.** Alternatively, cells without condensate may exhibit
 482 an imbalanced stoichiometry, where binding sites of the component of lower concentration are saturated with the
 483 component in excess. **f.** Cells are imaged, segmented, and cells with condensates are excluded. The concentrations of
 484 dimer (RFP, red), and tetramer (YFP, green) binding sites are recorded and plotted against each other. Both
 485 components are co-expressed stochastically, so each cell samples one point of the phase diagram. Scale bar: 10 μm **g.**
 486 *In vivo* phase diagram of our synthetic system containing wild-type Im2 and E9 interacting with a reported affinity
 487 of 15 nM (Table 1). Each point represents a single cell (n=6818) and shows binding site concentrations of the dimer
 488 (x-axis), and tetramer (y-axis). The red line highlights the diagonal. Grey dotted lines delimit background
 489 fluorescence levels below which concentrations cannot be estimated reliably (~ 3.5 nM). The yellow points show an
 490 overlay of the binodal computed based on the lattice model (Methods). The striped pattern visible at low
 491 concentrations along both axes is caused by the use of median intensity values, which results in discrete numbers.

492
 493 **Figure 3. Influence of affinity on phase separation *in vivo*.** **a.** Phase diagrams of the tetramer with the dimer
 494 carrying three different affinities, as indicated. The red line highlights the diagonal. The grey dotted lines indicate
 495 the fluorescence accuracy limit (~ 3.5 nM), below which autofluorescence increases. The yellow band highlights a
 496 region where phase separation occurs with wild type Im2, but does not with the high-affinity mutant. **b.** FRAP
 497 experiments were carried out for three pairs of components varying in their interaction affinity. Increasing the
 498 interaction affinity increased the effective viscosity of the condensate. Grey lines show individual repeats, the red
 499 line indicates the mean, red area shows the standard error. Sample sizes are indicated in each plot. **c.** Example of two
 500 condensates recovering after photobleaching. Low-affinity interaction (left) shows faster recovery when compared
 501 to condensates involving higher affinities (right). Scale bar: 5 μm .

502
 503 **Figure 4. Cotranslational binding of a nascent chain directs mRNA localization.** **a.** The mRNA of the dimeric
 504 component was tagged with the MS2 sequence, and appears in live cells as green fluorescent puncta²⁷. The
 505 tetrameric component did not contain YFP, so the condensates are shown with red fluorescence only. The mRNA
 506 molecules encoding for the dimer co-localize with the condensate. Scale bar: 5 μm . **b.** mRNAs of a control protein
 507 (GB1) do not colocalize with condensates. **c.** When the binding domain Im2 is encoded at the C-terminus of the
 508 dimer, the mRNA does not co-localize with the condensate. **d.** Quantification of experiments depicted in panels a-c.
 509 Cells were automatically segmented from brightfield microscopy images. When foci were detected in both (red and
 510 green) channels, their distance was calculated from the coordinates of the brightest detected foci in the maximum z-
 511 projection of seven stacks. Boxes delineate the first and third quartiles, the black line corresponds to the median,
 512 upper and lower whiskers extend to largest and smallest values and at most 1.5 times the interquartile range. P-
 513 values are indicated above (one-sided t-test). **e.** Puromycin treatment dissociates ribosomes from mRNA and
 514 releases the dimers' mRNA from the condensate. **f.** Puromycin-induced dissociation of mRNA does not occur when
 515 cycloheximide, a drug that inhibits puromycin-dependent run-off of polysomes, is co-administered with puromycin.
 516 **g.** Quantification of experiments depicted in panels d and e. Cells exhibiting co-localization of mRNA and condensate
 517 were followed after treatment with either puromycin alone, or co-administered with cycloheximide for 25 minutes.
 518 The fraction of cells exhibiting complete detachment of the mRNA punctae from the condensates is shown. Error
 519 bars represent one standard deviation of the mean.

522 Tables

523
 524 **Table 1. Im2 variants previously reported and used to modulate the interaction affinity between the dimer**
 525 **and tetramer.** Previously reported²¹ mean and standard errors of the affinities are given (n=2). Mutants marked
 526 with a triangle[▲]were added later in this work. For those, we derived phase-diagrams only.

Im2 mutation	K_d with E9 (M)
D33L N34V R38T [▲]	$3.4 \pm 1.4 \times 10^{-13}$
D33L	$4.8 \pm 0.3 \times 10^{-11}$
N34V R38T [▲]	$1.9 \pm 0.4 \times 10^{-10}$

R38T ▲	$2.6 \pm 0.5 \times 10^{-9}$
N34V ▲	$3.3 \pm 0.7 \times 10^{-9}$
WT	$1.5 \pm 0.1 \times 10^{-8}$
E30A	$2.8 \pm 1.6 \times 10^{-7}$
P56A	$2.1 \pm 0.7 \times 10^{-6}$
V37A	$9.3 \pm 4.4 \times 10^{-6}$

528 **Methods**

529 *Design*

530 The synthetic system introduced in this work relies on homo-oligomerization to create multivalent
531 components. We chose specific homo-oligomerization domains so as to avoid intra-molecular interactions
532 between components. Specifically, we selected a large dimer and a small tetramerization domain such
533 that the dimers could bridge across two tetramers, but could not bind two sites on the same tetramer. The
534 dimer consists of an antiparallel coiled-coil, where both N- termini are 18 nm apart. The tetramer is
535 comparatively small and corresponds to the tetramerization domain of p53 (details of protein structures
536 and references appear in Supplementary Table 1).

537
538 To avoid non-specific interactions of the dimer protein we mutated highly exposed and hydrophobic
539 surface residues to charged ones (Y22D, I92D). For the tetrameric component, we used the wild-type
540 sequence of the tetramerization domain of human p53, from amino acid 326 to 356. The yellow
541 fluorescent reporter was fused to the tetramer, and the red fluorescent protein to the dimer (details of
542 fluorescent proteins and references appear in Supplementary Table 1). Both fluorescent proteins used are
543 monomeric to prohibit unspecific interactions between the components. The interaction domains were
544 derived from the bacterial toxin-antitoxin system E9/Im2. Different affinities were achieved by
545 introducing point mutations in the sequence of Im2 (Table 1). An H103A mutant of E9 was used to inhibit
546 its toxic DNase activity. Upon initial expression in yeast cells, the dimer component showed a tendency
547 for nuclear localization. We thus fused a nuclear export signal (NES) LAEKLGLDIN at its N-terminus,
548 which led to its cytosolic localization.

549 *Plasmids and Strains*

550 The plasmids and strains resulting from this work are described in Supplementary Tables 2 and 3.

551
552 To achieve a stochastic expression of each component in yeast cells, each ORF was inserted into a
553 separate low copy centromeric plasmid. The tRNA adaptation index of sequences for all components was
554 optimized for *S. cerevisiae*. Designed sequences were inserted into American Type Culture Collection
555 (ATCC) yeast cassettes⁵¹ using the Polymerase Incomplete Primer Extension (PIPE) cloning method⁵². For
556 stoichiometric expression in Video 1, sequences were inserted into M3925 plasmids⁵³ for genomic
557 integration. Both components were cloned downstream of the yeast *TDH3* promoter. The selection
558 markers for the dimer and tetramer were hygromycin and G418, respectively. Cloning was performed in

559 *E. coli* DH5 α cells. Plasmids were subsequently isolated, verified by sequencing, and transformed into
560 BY4741 (tetramer) or BY4742 (dimer) strains of S288C⁵⁴. Expression in haploid cells was verified by
561 microscopy and yeast were subsequently mated, creating diploid cells containing both plasmids. For
562 investigating the localization of mRNA, a modified version of the mTAG method²⁷ was used. Instead of
563 inserting the MS2 loops to the 3'UTR by using the Cre-Lox system, we used CRISPR/Cas9. We used the
564 plasmid bRA89⁵⁵, which carries both, the ORF for Cas9, and the guide RNA. The guide RNA was designed
565 using CRISPR-ERA⁵⁶, to target the *TRP3* locus (GTGGACAATCTCACCAGCGT) and the dimer with the wild
566 type Im2, including the MS2 loops in its 3' untranslated region (UTR), was inserted. For the insertion
567 cassette, three pieces were amplified: one from the promoter to the stop codon, one from the stop codon
568 to the end of UTR containing 12 MS2 loop repeats, and one from the end of the 3' UTR to the end of the
569 terminator. The primers for this amplification contained 40 bp homology regions to the *TRP3* locus on the
570 flanking regions, and to each other in overlapping regions. The PCR products were treated with DPN1
571 (New England Biolabs inc.) and purified using the Agencourt AMPure XP system. We transformed 20 μ l of
572 competent BY4742 cells with 1 μ l (1 μ g/ μ l) bRA89 (*TRP3*) and 200-300 ng of each module of the
573 insertion cassette. After inserting the dimer, cells were cotransformed with the plasmid carrying CP-
574 3xGFP and a plasmid carrying the tetramer fused to mTagBFP2, instead of Venus. For the negative
575 control, the insertion cassette consisted of three fragments: one with the *TDH3* promoter and GB1, one
576 with the MS2L containing 3' UTR and one with the *CYC* terminator (please refer to Supplementary Table
577 1, 2 and 3 for references of the proteins used in these constructs). The three fragments were purified with
578 the Agencourt AMPure XP system, joined by PCR, and the resulting piece was again purified. 500 ng of the
579 product was cotransformed with 1 μ g of bRA89 (*TRP3*) to 20 μ l competent BY4742 cells. The resulting
580 strain was cotransformed with the CP-3xGFP plasmid as well as the plasmids for the dimer and the BFP-
581 tagged tetramer. Finally, all strains were verified by sequencing. We note that one of the 12 MS2 loops
582 was missing in the negative control. However, mRNAs were clearly visible in that strain, allowing us to
583 unambiguously assess their co-localization with condensates.

584 ***Microscopy and Image Processing***

585 Cells were imaged with an Olympus IX83 microscope coupled to a Yokogawa CSU-W1 spinning disc
586 confocal scanner with dual Hamamatsu ORCA-Flash4.0 V2 sCMOS cameras. 16-bit images were acquired
587 for Brightfield and two confocal illumination schemes: GFP channel (Ex 488 nm, Toptica 100 mW | Em
588 525/50 nm, Chroma ET/m), and RFP channel (Ex 561 nm, Obis 75 mW | Em 609/54 nm, Chroma ET/m).
589 Imaging was performed with a 60x, 1.35 NA, oil immersion objective (UPLSAPO60XO, Olympus) and
590 FRAP experiments were carried out with a 100x, 1.4 NA, oil-immersion objective (UPLSAPO100XO,
591 Olympus). Automated imaging was performed with a motorized XY stage, onto which a piezo-stage (Mad
592 City Labs) was mounted and used for acquiring z-stacks. For phase diagrams, we acquired seven z-stack
593 images for each fluorescent channel, and the average intensity projection was used. For time-lapse series,
594 eight z-stacks were acquired, and the maximum intensity projection was used.

595 ***Sample preparation for imaging***

596 A liquid handling robot (Tecan Evo 200) was used to prepare Greiner™ 384-well glass-bottom optical
597 imaging plates. For imaging, 0.5 μ l of saturated cell suspension was transferred into an optical plate with
598 SD medium and grown for 6 h to logarithmic growth. For time-lapse series, cells were grown to an OD600
599 of 0.4-0.8, transferred to matrical 96-well glass-bottom plates, and covered with 0.5% Agarose/SD
600 containing the respective resistance marker. For time-lapse series of puromycin treatment, cells were not
601 covered with agarose, and puromycin was added to the cells after 6 minutes of imaging, to a final

602 concentration of 10 mM. For treatment with puromycin and cycloheximide, a mixture of the drugs was
603 added to yield a final concentration of 10 mM puromycin and 100 ug/ml cycloheximide. For FRAP
604 experiments, cells were grown and let at saturation for two weeks to generate large condensates. Cells
605 were subsequently fixed with ConA in an optical 96-well plate, as previously described⁵⁷, and FRAP
606 experiments were carried out 6 h after their inoculation into fresh media.

607 ***Image analysis and generation of in vivo phase diagrams***

608 Cells were identified, segmented, and their fluorescent signal (median, average, minimum, maximum,
609 10th, 20th, ..., 90th percentile fluorescence) as well as additional cell properties were identified using
610 custom algorithms⁵⁸ in ImageJ/FIJI⁵⁹, and exported as tabulated files. Condensates were identified in each
611 cell independently, in a multistep process: (i) we calculated the median fluorescence intensity of pixels in
612 a given cell. (ii) we identified the largest region composed of pixels with an intensity 3-fold above the
613 median. If such a region existed, showed a circularity above 0.4 and an area above 9 pixels, the cell was
614 deemed to contain a condensate.

615 Tabulated data resulting from image analyses were loaded and analyzed with custom scripts in R. To
616 convert fluorescent intensities to cytosolic concentrations, His-tagged Venus and FusionRed were purified
617 using the GE Healthcare His GraviTrap system. Serial dilutions of each protein were generated,
618 fluorescence intensities were recorded, and a linear model was fitted (Supplementary Figure 1). A
619 fluorescent plastic slide (Chroma Technology) served as a constant reference to calibrate fluorescence
620 signals of experiments carried out on different days. Fluorescence signals of the experiments were
621 normalized according to the fluorescent slide and cytosolic concentrations were inferred from the
622 regression of the purified proteins. Finally, cells with condensates were excluded, and the median
623 cytosolic concentrations of YFP and RFP were plotted against each other.

624 ***Fluorescence recovery after photobleaching (FRAP)***

625 A macro created in VisiView 4.4 ® software was written to capture images on the red channel in rapid
626 succession during the course of a FRAP experiment. Photobleaching was achieved with a 405 nm laser
627 pulse lasting 20 ms after the 10th frame of the acquired series. The RFP channel exposure was set to 50
628 ms. Images were acquired every 100 ms. 250 frames for a total acquisition time of 25 seconds were
629 acquired.

630 ***Lattice model of dimers and tetramers***

631 The tetramer-dimer attraction is the only interaction energy in this simplified lattice model. Nearest-
632 neighbor tetramers or dimers separated by solvent molecules do not interact. Higher-order neighbor
633 interactions are neglected and the zero of energy is set by the tetramer-solvent and dimer-solvent
634 interactions, which we take to be equal for simplicity. The thermodynamic criterion for coexistence is an
635 equal chemical potential and osmotic pressure for each of the species (tetramer, dimer and solvent
636 molecules) in the two phases. The model captures these effects to predict the concentration, temperature,
637 and binding strength regimes where phase separation occurs. A mean-field theory and calculation that
638 results in the phase diagrams shown in the main text are described in Ref. ⁶⁰.

639 The experimental data corresponding to the interaction 1.5×10^{-8} M is about $18 k_B T$ (Fig. 2g). The lattice
640 model involves solving four nonlinear algebraic equations to find the equilibrium concentrations of the
641 complexes and then using interpolation we find the analytical expression for the free energy that we
642 finally use to find the binodal phase diagram numerically. This procedure makes it hard to numerically

643 find the binodal for very large interaction strengths. The theory shows that the minima of the phase
644 diagrams vary exponentially with the interaction strength⁶⁰. For these reasons, we show an overlay of the
645 theoretical binodal (and not a fit) on the experimental data.

646 **FRAP data analysis**

647 Custom macros were created in ImageJ/FIJI⁵⁹ to extract quantitative data from the image series. Data
648 were extracted from the non-bleached area and the bleached area by first manually selecting two pixel
649 coordinates, first at the center of the bleached region and second at the center of the non-bleached region.
650 Then, a circular region of interest (ROI) of 6 pixels in diameter was generated. Since small movements of
651 the condensate can occur when recording the video, we generated 42 additional adjacent ROIs by
652 translation of either 0.5, 1, 1.5 or 2 pixels in all directions, generating 6, 8, 12, or 16 ROIs for each distance
653 respectively. Then, the average intensity of each ROI was extracted for every frame of the image series.
654 The ROI intensities were subsequently analyzed with custom scripts in R. First, for each of the two
655 locations (bleached and unbleached), we averaged 5 sub-ROIs showing either the lowest (bleached area)
656 or highest total fluorescence intensity (non-bleached area). For each frame, the intensity recorded for the
657 bleached area was divided by the intensity of the non-bleached area. Finally, the values were normalized
658 as follows: $x_{norm} = \frac{x - x_{min}}{\max(x - x_{min})}$, where x is the ratio of integrated pixel intensities measured in the
659 bleached over unbleached ROI, and x_{min} is the minimum value of x across the image series.
660

661

662 **Data availability**

663 We provide single-cell measurements of YFP and RFP concentrations for all phase diagrams in a
664 supplementary Excel table. Other data are available from the authors upon request.

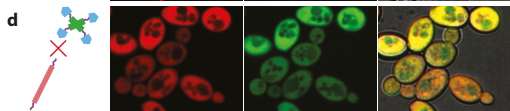
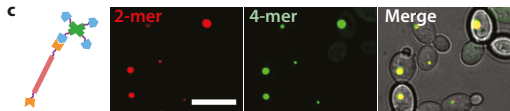
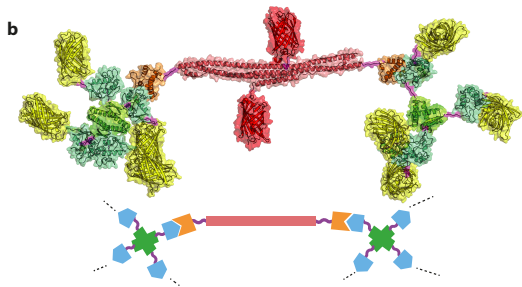
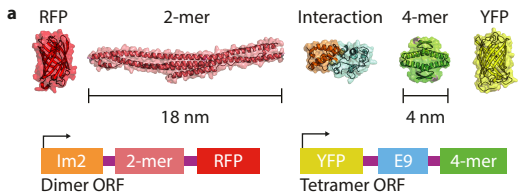
665 **Code availability**

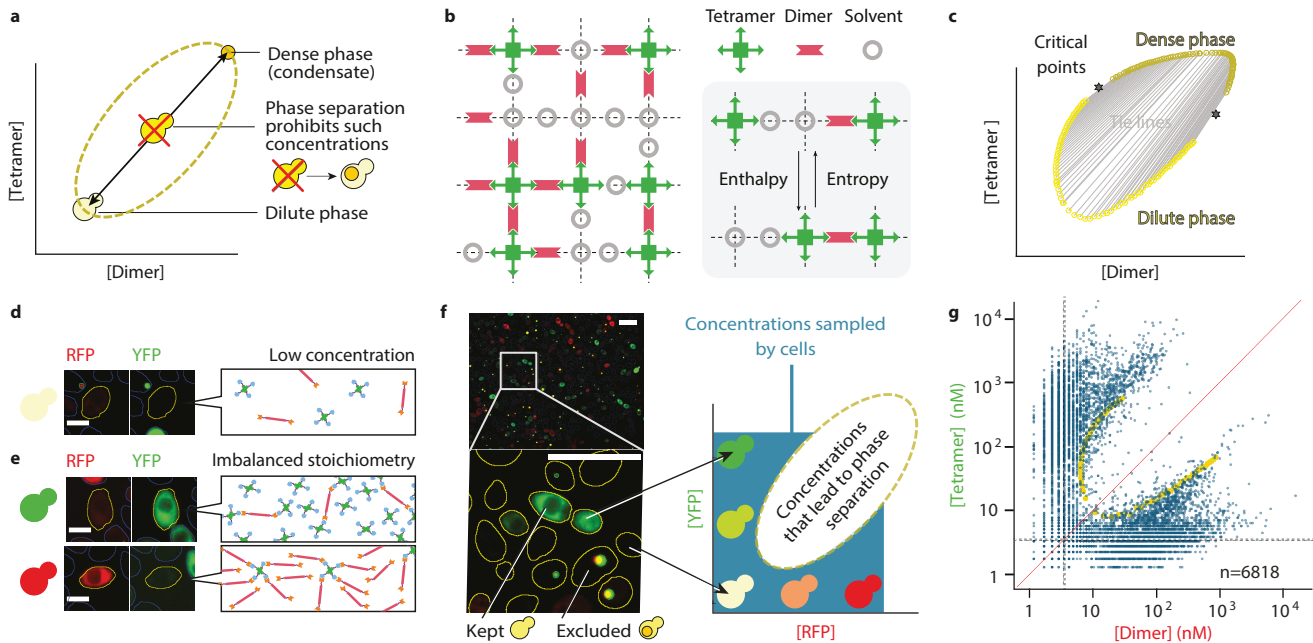
666 Code and custom scripts used in this work are available from the authors upon request. We used the open
667 source package oxDNA (version 2.4) to run the sedimentation simulations.
668

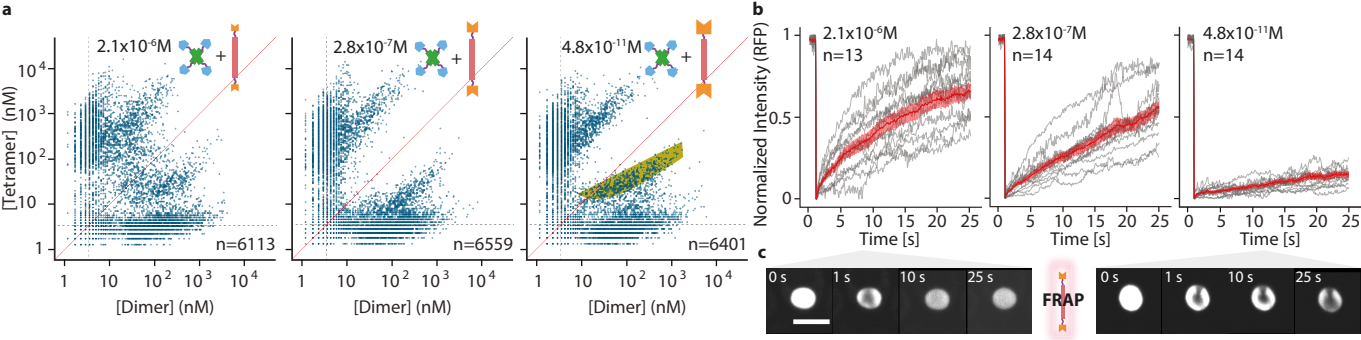
669 **References (Methods)**

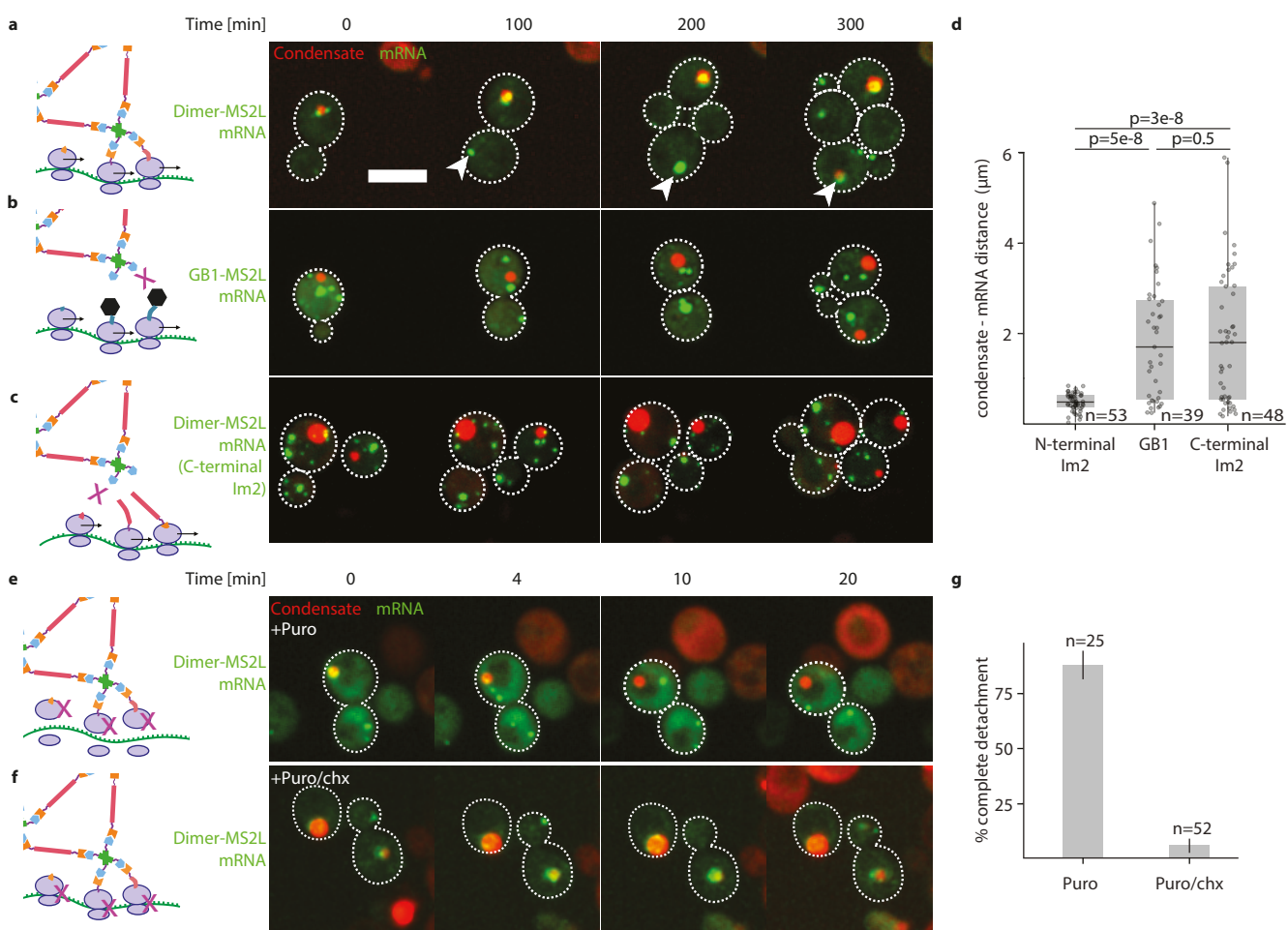
- 670 51. Mumberg, D., Müller, R. & Funk, M. Yeast vectors for the controlled expression of
671 heterologous proteins in different genetic backgrounds. *Gene* **156**, 119–122 (1995).
672 52. Klock, H. E. & Lesley, S. A. The Polymerase Incomplete Primer Extension (PIPE) method
673 applied to high-throughput cloning and site-directed mutagenesis. *Methods Mol. Biol.* **498**, 91–103
674 (2009).
675 53. Voth, W. P., Jiang, Y. W. & Stillman, D. J. New ‘marker swap’ plasmids for converting
676 selectable markers on budding yeast gene disruptions and plasmids. *Yeast* **20**, 985–993 (2003).
677 54. Brachmann, C. B. *et al.* Designer deletion strains derived from *Saccharomyces cerevisiae*
678 S288C: a useful set of strains and plasmids for PCR-mediated gene disruption and other applications.
679 *Yeast* **14**, 115–132 (1998).
680 55. Anand, R., Beach, A., Li, K. & Haber, J. Rad51-mediated double-strand break repair and

681 mismatch correction of divergent substrates. *Nature* **544**, 377–380 (2017).
682 56. Liu, H. *et al.* CRISPR-ERA: a comprehensive design tool for CRISPR-mediated gene editing,
683 repression and activation. *Bioinformatics* **31**, 3676–3678 (2015).
684 57. Cohen, Y. & Schuldiner, M. Advanced Methods for High-Throughput Microscopy Screening
685 of Genetically Modified Yeast Libraries. in *Methods in Molecular Biology* 127–159 (2011).
686 58. Matalon, O., Steinberg, A., Sass, E., Hausser, J. & Levy, E. D. Reprogramming protein
687 abundance fluctuations in single cells by degradation. *bioRxiv* (2018) doi:10.1101/260695.
688 59. Schindelin, J. *et al.* Fiji: an open-source platform for biological-image analysis. *Nat. Methods*
689 **9**, 676–682 (2012).
690 60. Nandi, S. K., Heidenreich, M., Levy, E. D. & Safran, S. A. Interacting multivalent molecules:
691 affinity and valence impact the extent and symmetry of phase separation. *arXiv 1910.11193* (2019).
692









Affinity
for E9
[M]

None

3×10^{-5}

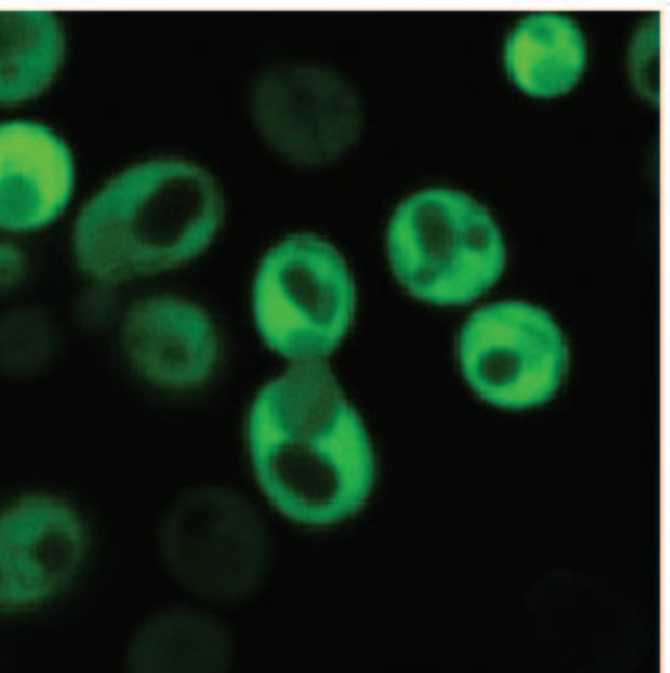
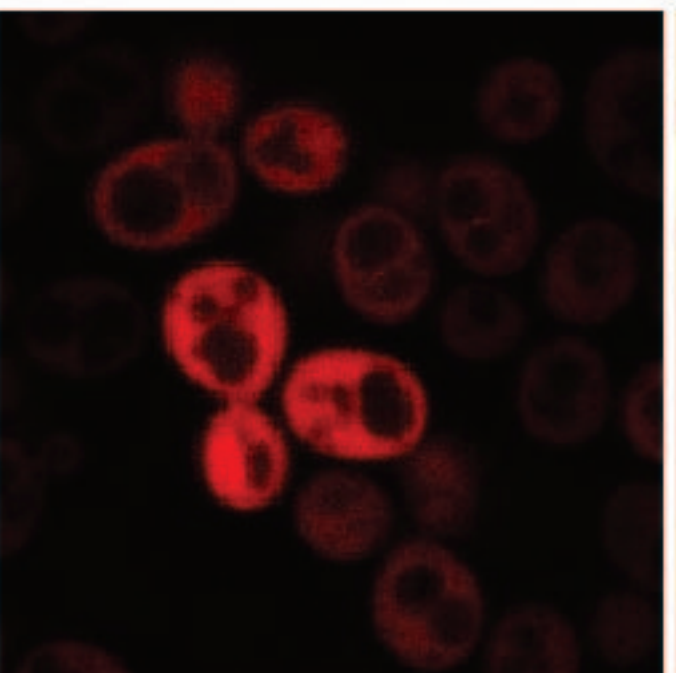
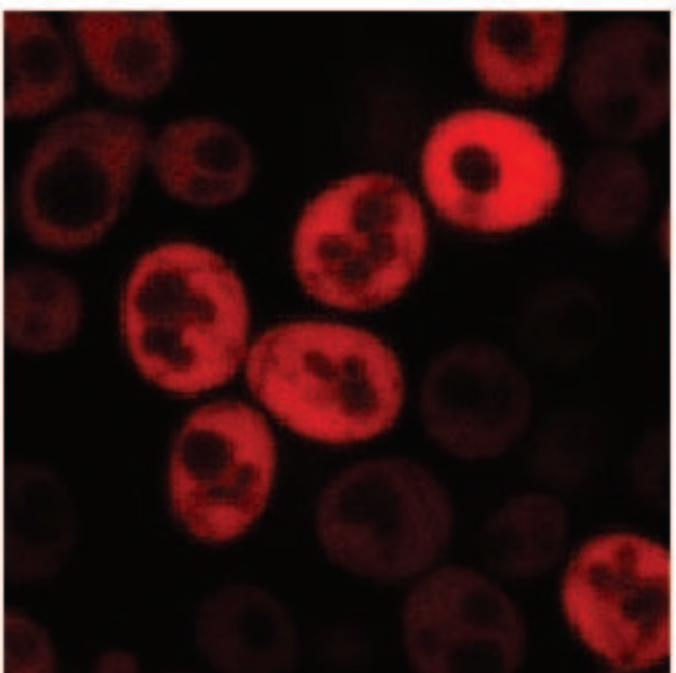
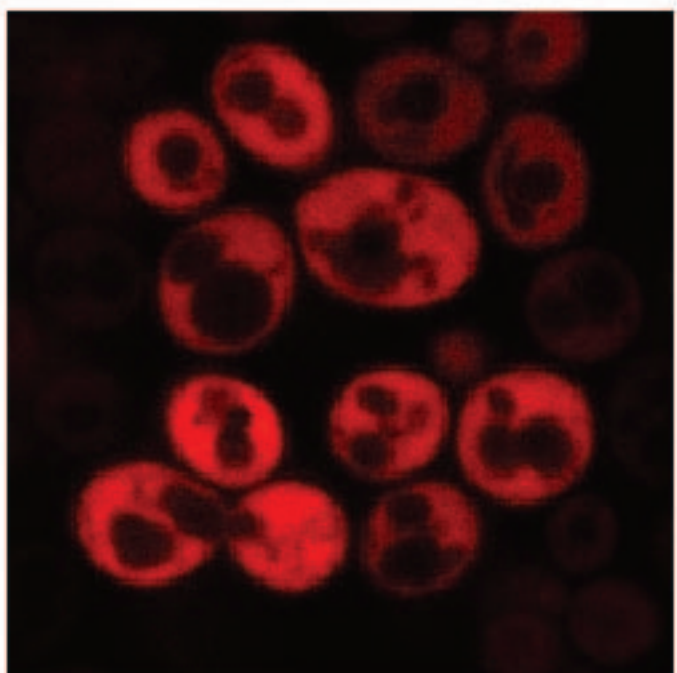
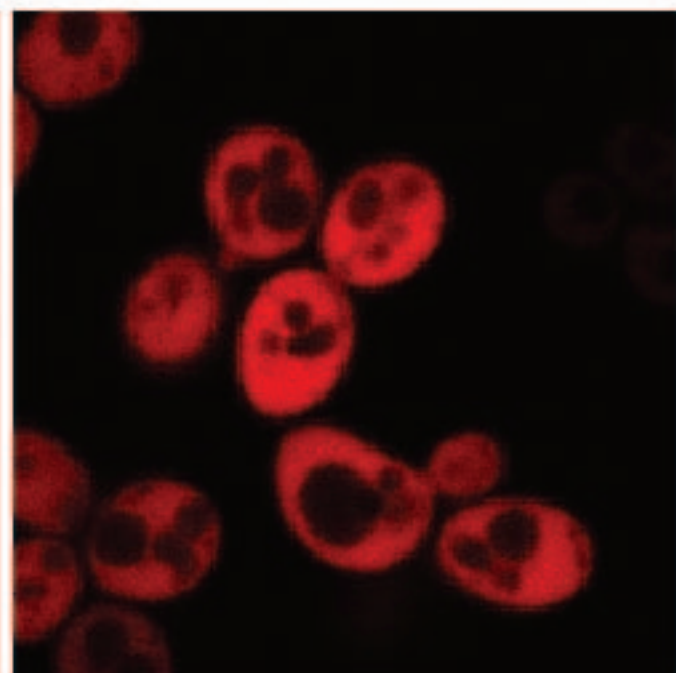
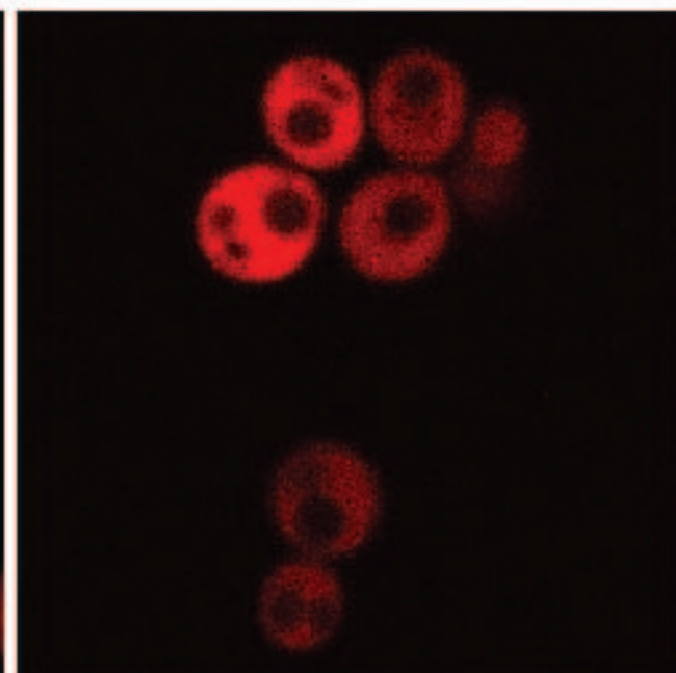
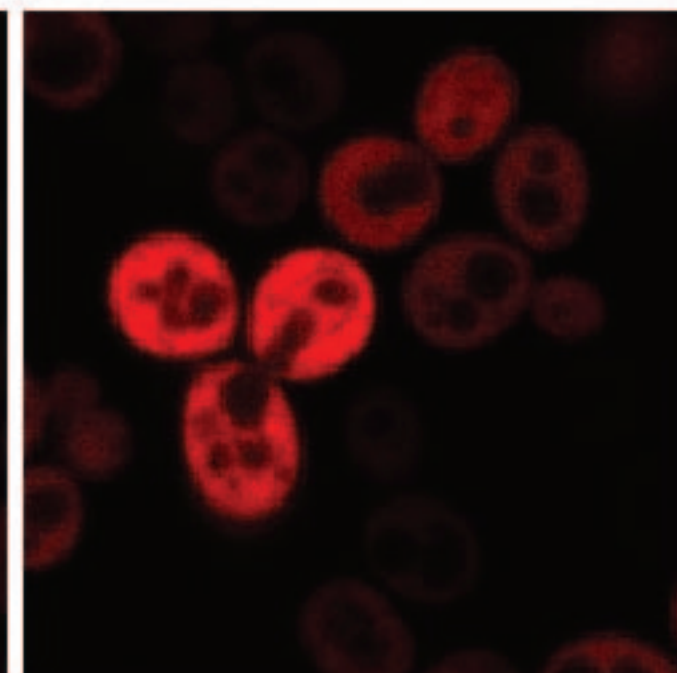
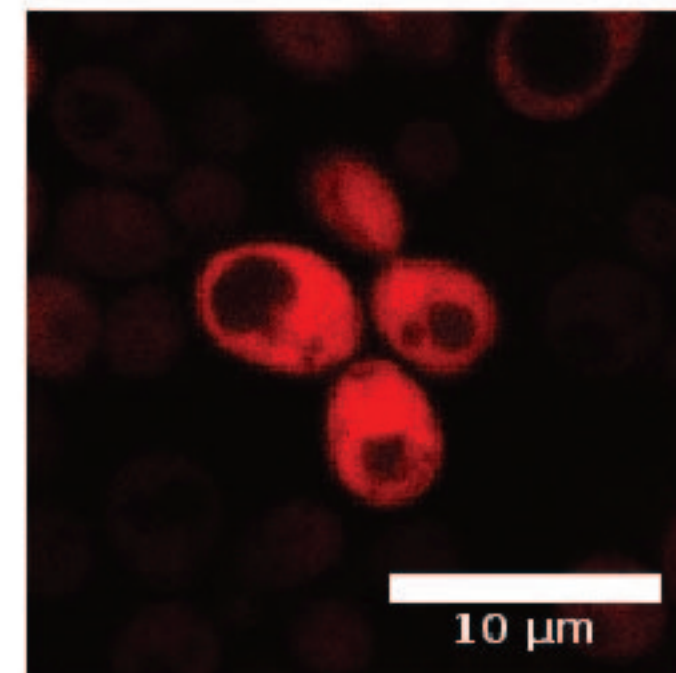
2.1×10^{-6}

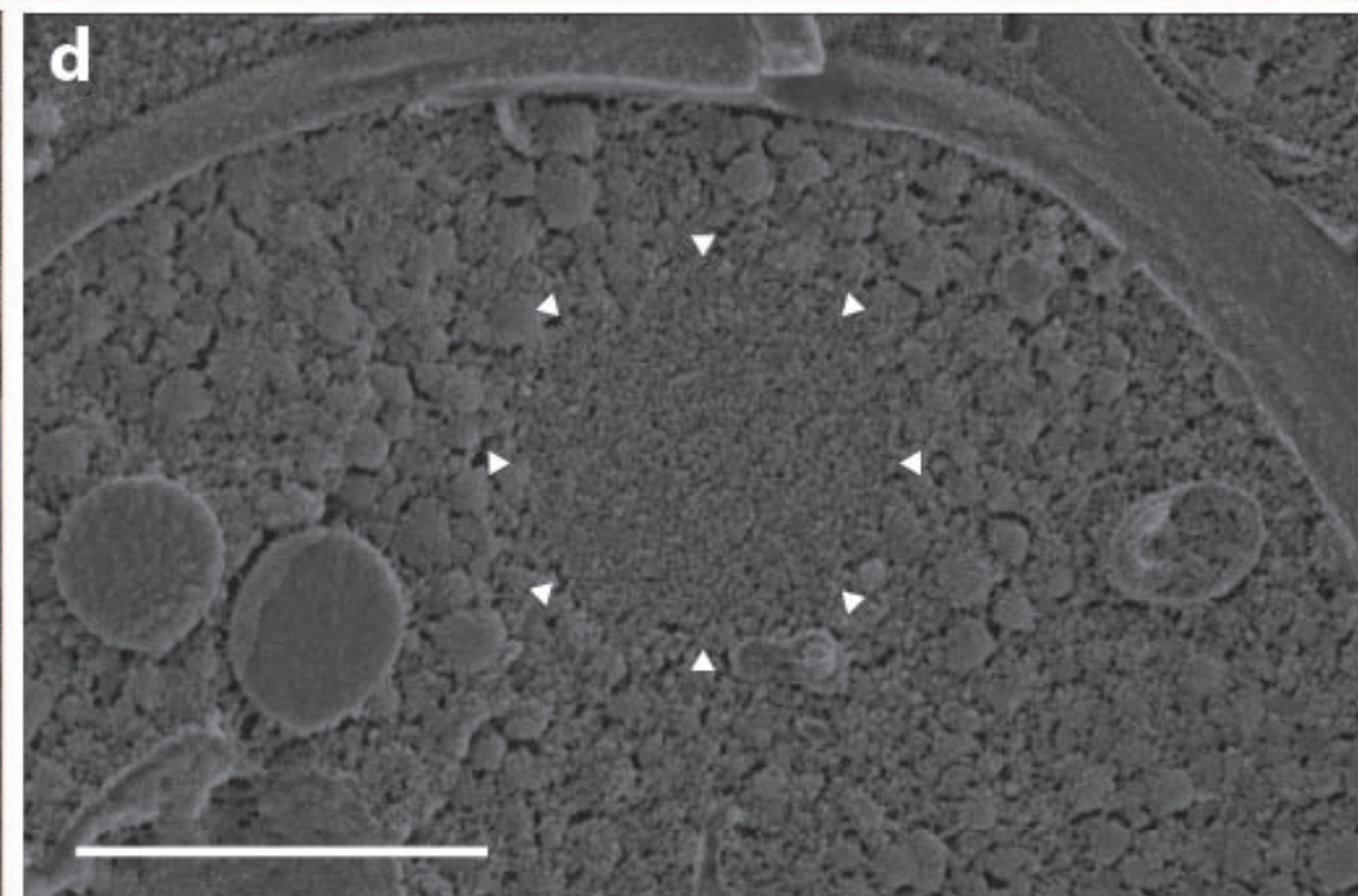
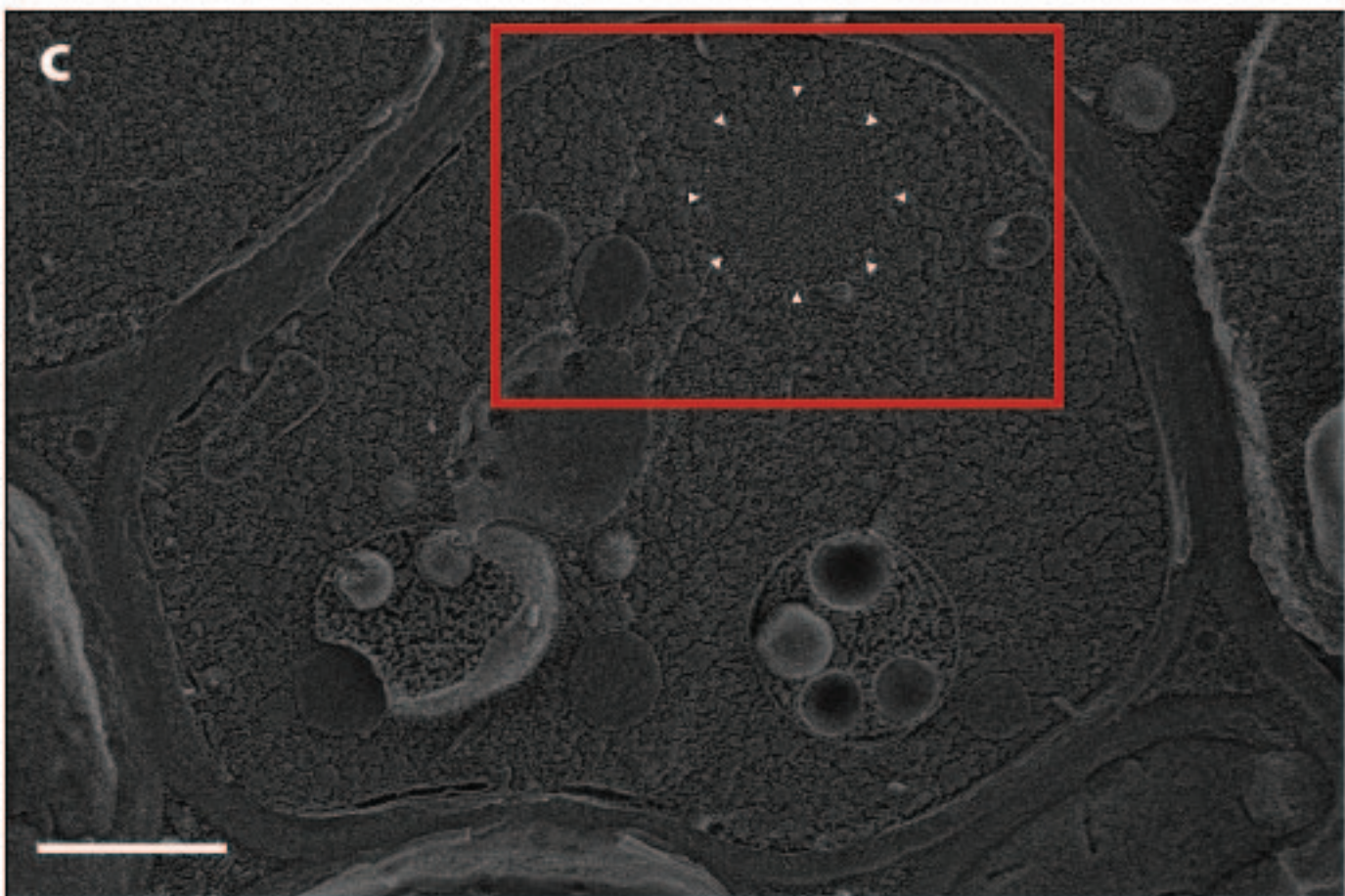
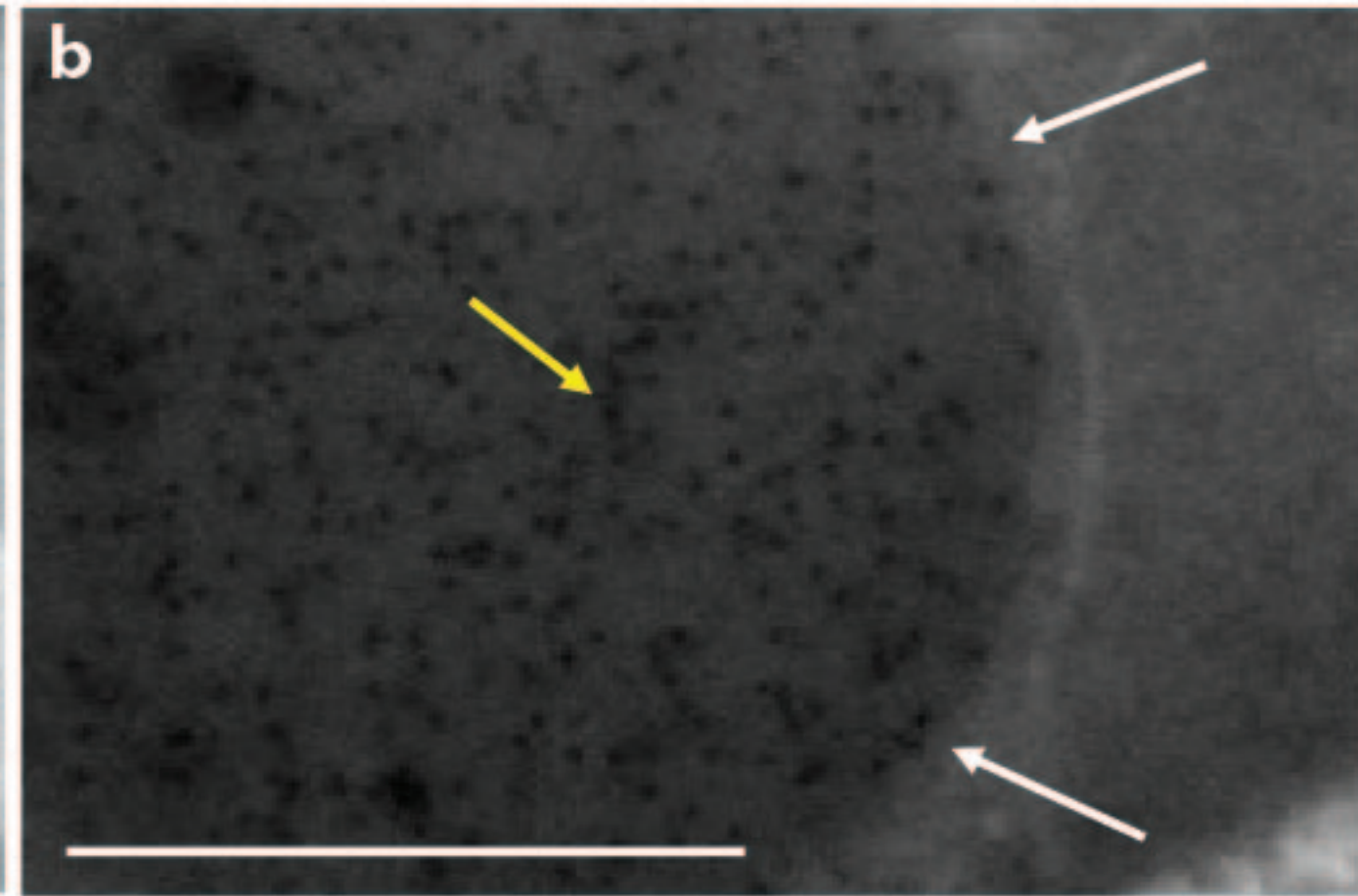
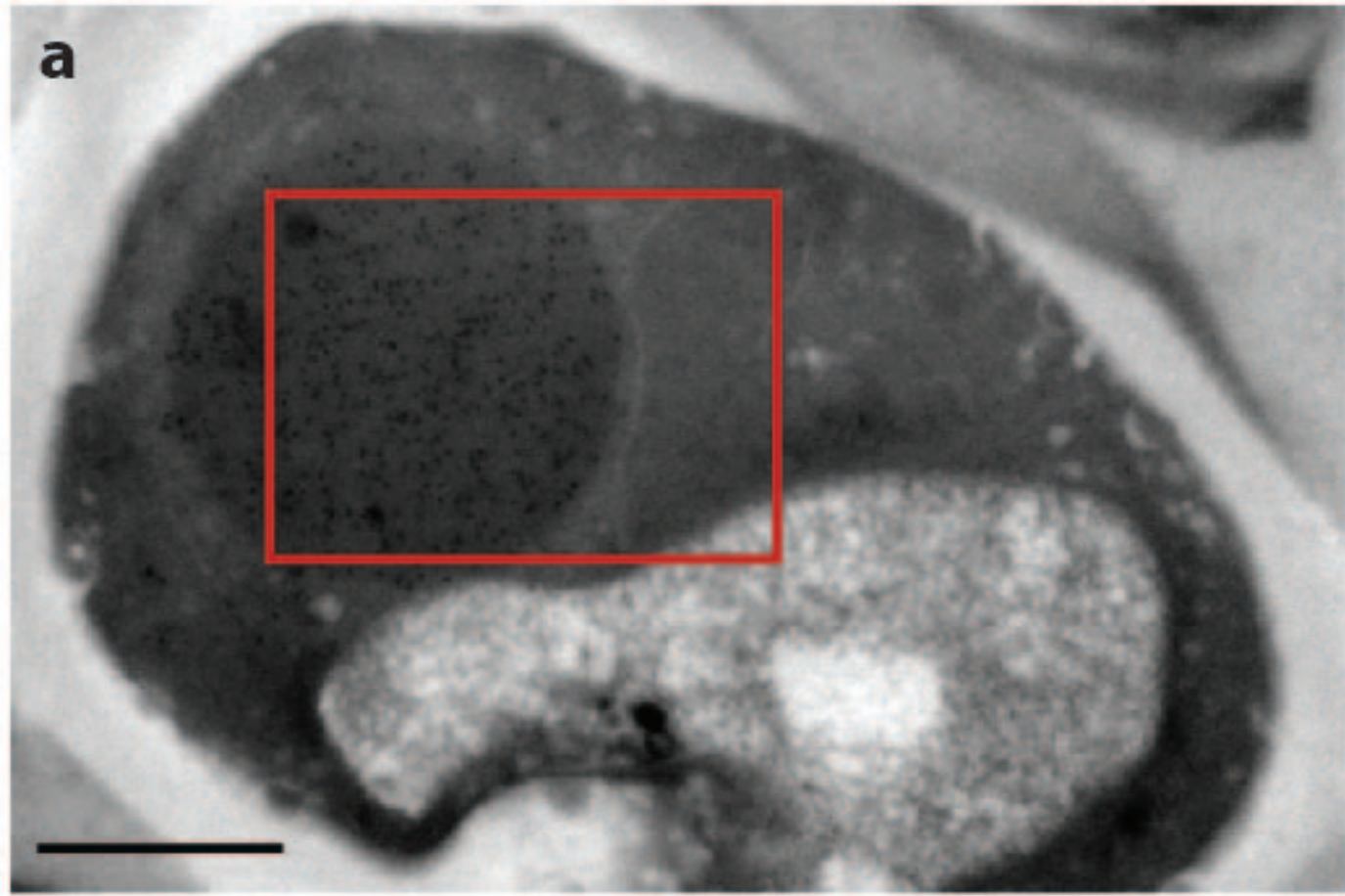
9.3×10^{-6}

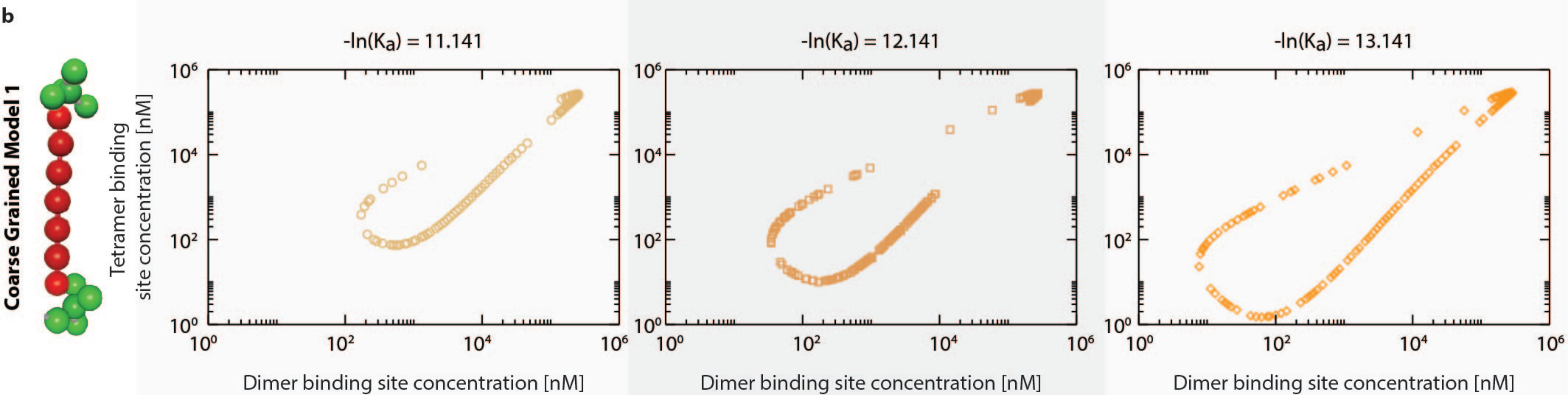
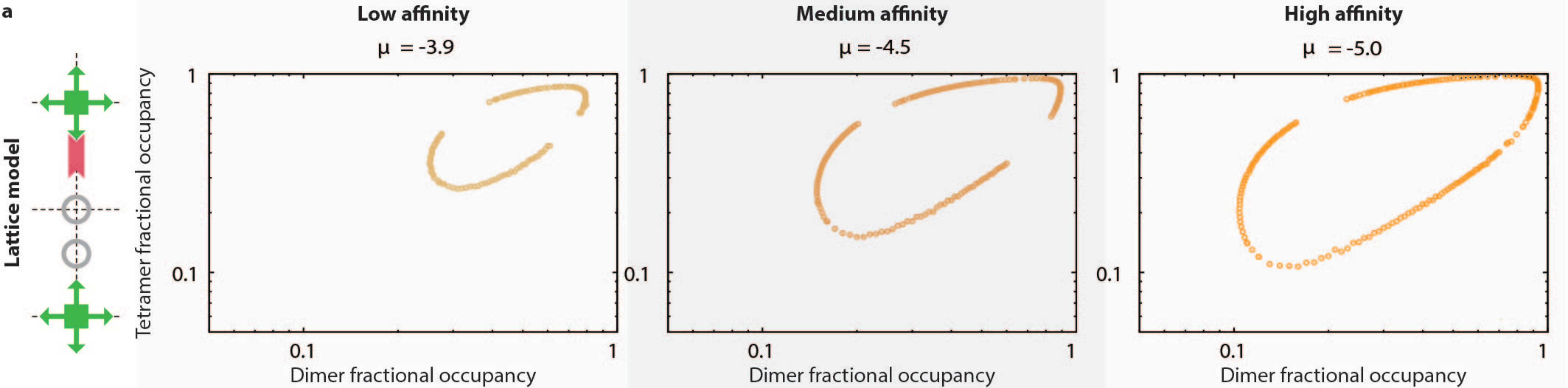
2.8×10^{-7}

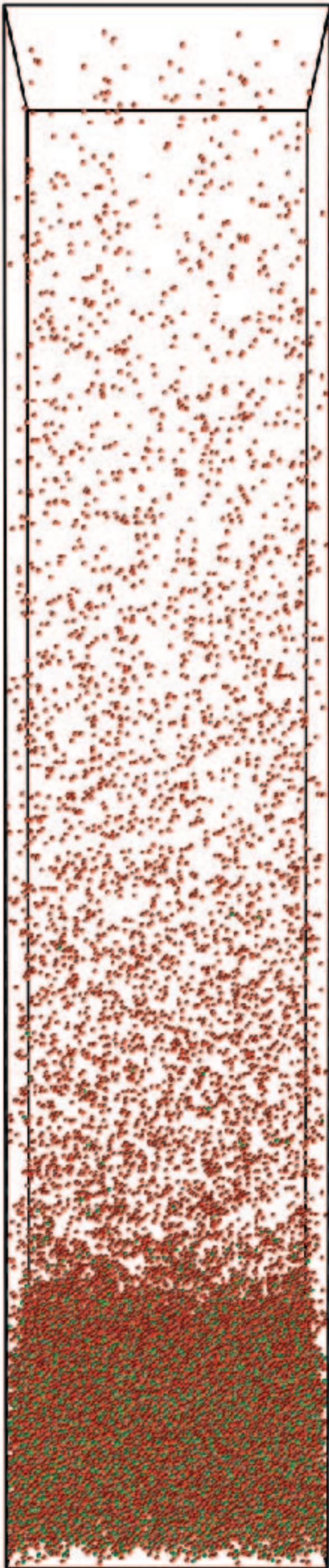
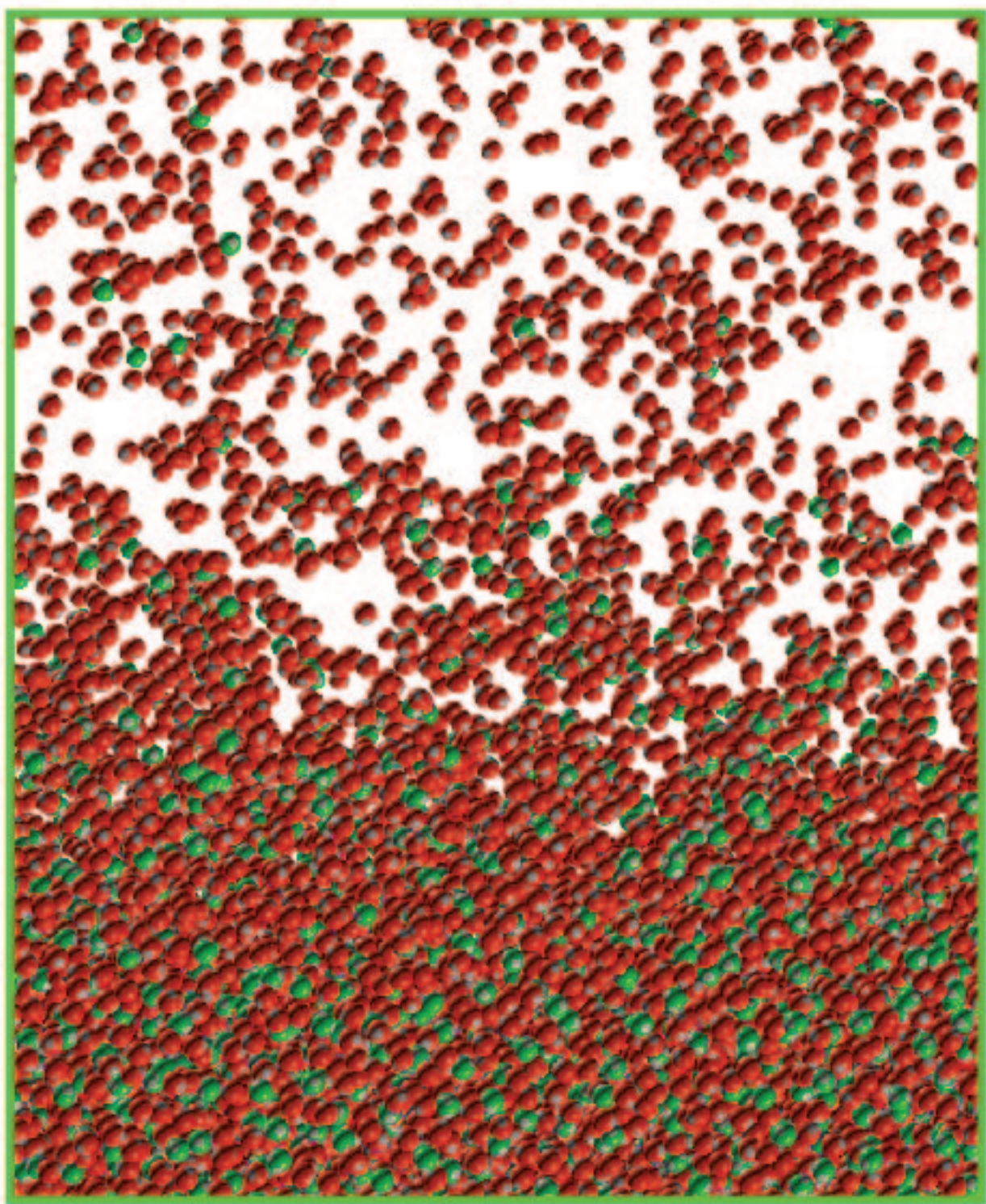
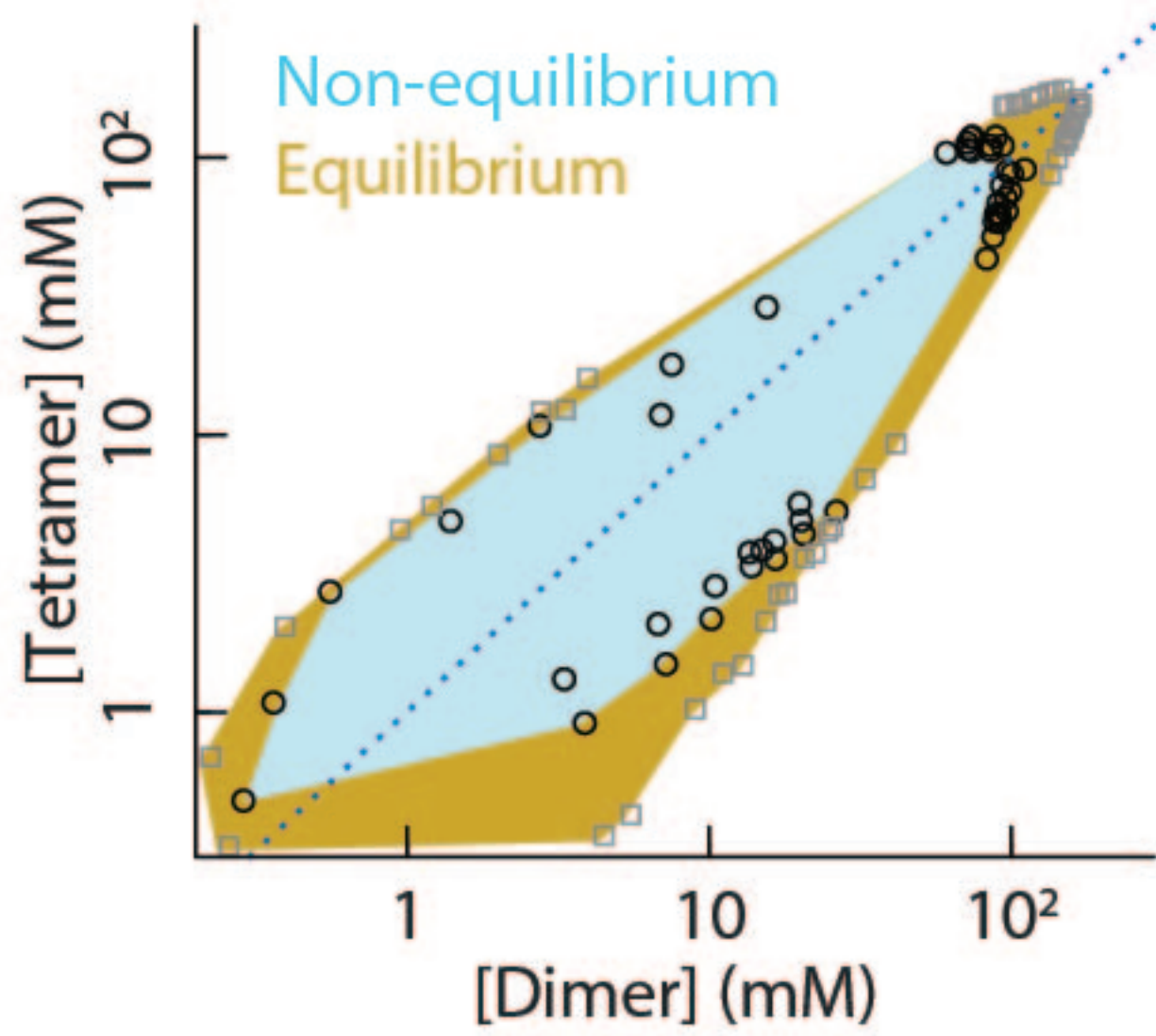
1.5×10^{-8}

4.8×10^{-11}

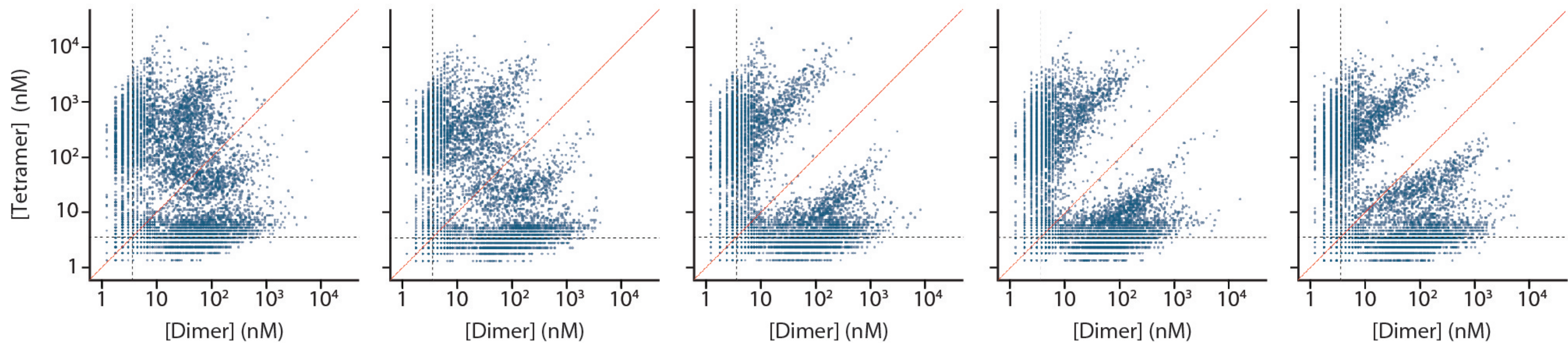
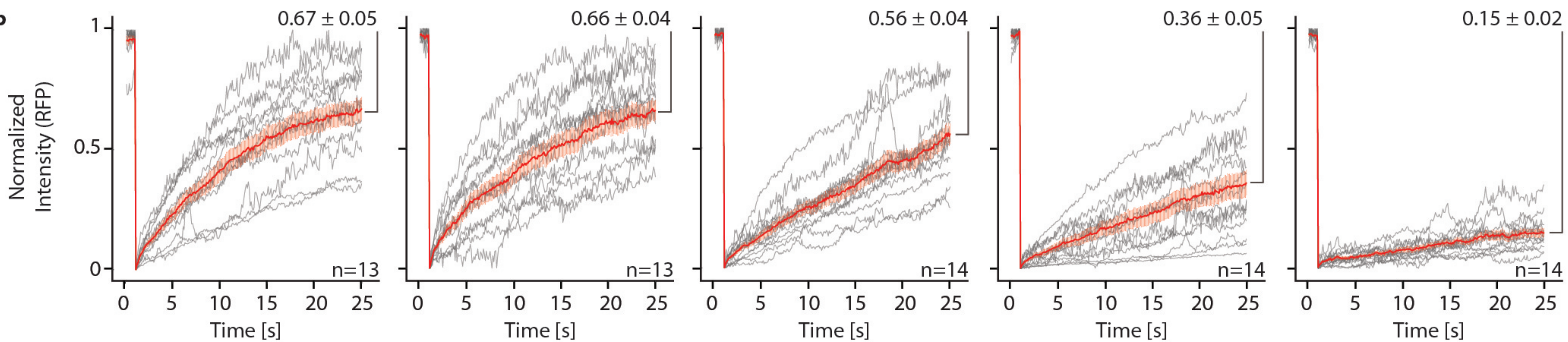






a**b**

Affinity

a**b**

Im2 mutant

Affinity (M)

V37A

9.3×10^{-6}

P56A

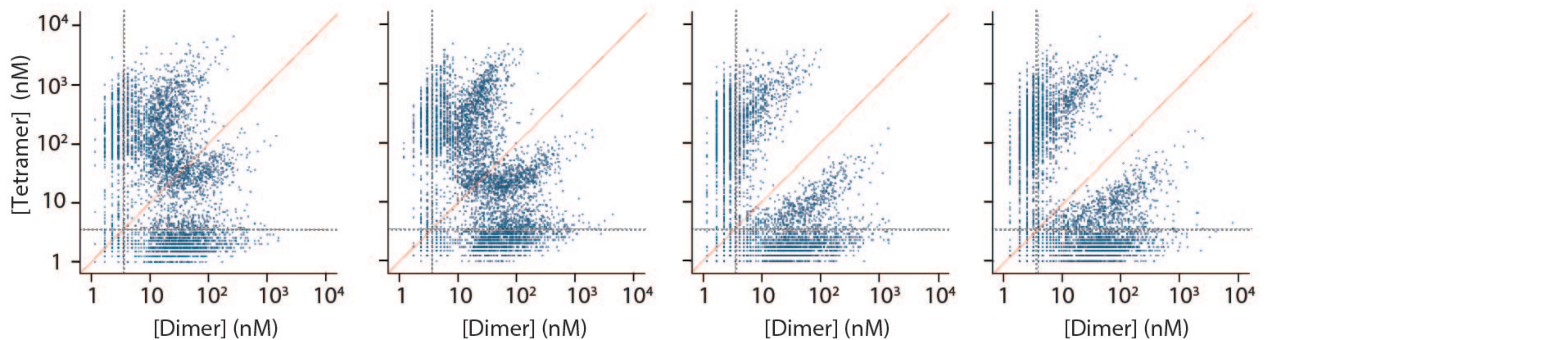
2.1×10^{-6}

E30A

2.8×10^{-7}

wt

1.5×10^{-8}



Im2 mutant

Affinity (M)

N34V

3.3×10^{-9}

R38T

2.6×10^{-9}

N34V R38T

1.9×10^{-10}

D33L

4.8×10^{-11}

D33L N34V R38T

3.4×10^{-13}

